NASA/TM—2016-219137 AIAA–2016–3733

Ice-Accretion Test Results for Three Large-Scale Swept-Wing Models in the NASA Icing Research Tunnel

Andy P. Broeren and Mark G. Potapczuk
Glenn Research Center, Cleveland, Ohio

Sam Lee
Vantage Partners, LLC, Brook Park, Ohio

Adam M. Malone and Bernard P. Paul, Jr.
Boeing Commercial Airplanes, Seattle, Washington

Brian S. Woodard
University of Illinois at Urbana-Champaign, Urbana, Illinois

September 2016

NASA STI Program . . . in Profile

Since its founding, NASA has been dedicated to the advancement of aeronautics and space science. The NASA Scientific and Technical Information (STI) Program plays a key part in helping NASA maintain this important role.

The NASA STI Program operates under the auspices of the Agency Chief Information Officer. It collects, organizes, provides for archiving, and disseminates NASA's STI. The NASA STI Program provides access to the NASA Technical Report Server—Registered (NTRS Reg) and NASA Technical Report Server—Public (NTRS) thus providing one of the largest collections of aeronautical and space science STI in the world. Results are published in both non-NASA channels and by NASA in the NASA STI Report Series, which includes the following report types:

- TECHNICAL PUBLICATION. Reports of completed research or a major significant phase of research that present the results of NASA programs and include extensive data or theoretical analysis. Includes compilations of significant scientific and technical data and information deemed to be of continuing reference value. NASA counter-part of peer-reviewed formal professional papers, but has less stringent limitations on manuscript length and extent of graphic presentations.

- TECHNICAL MEMORANDUM. Scientific and technical findings that are preliminary or of specialized interest, e.g., "quick-release" reports, working papers, and bibliographies that contain minimal annotation. Does not contain extensive analysis.

- CONTRACTOR REPORT. Scientific and technical findings by NASA-sponsored contractors and grantees.

- CONFERENCE PUBLICATION. Collected papers from scientific and technical conferences, symposia, seminars, or other meetings sponsored or co-sponsored by NASA.

- SPECIAL PUBLICATION. Scientific, technical, or historical information from NASA programs, projects, and missions, often concerned with subjects having substantial public interest.

- TECHNICAL TRANSLATION. English-language translations of foreign scientific and technical material pertinent to NASA's mission.

For more information about the NASA STI program, see the following:

- Access the NASA STI program home page at http://www.sti.nasa.gov

- E-mail your question to help@sti.nasa.gov

- Fax your question to the NASA STI Information Desk at 757-864-6500

- Telephone the NASA STI Information Desk at 757-864-9658

- Write to:
  NASA STI Program
  Mail Stop 148
  NASA Langley Research Center
  Hampton, VA 23681-2199

NASA/TM—2016-219137 AIAA–2016–3733

Ice-Accretion Test Results for Three Large-Scale Swept-Wing Models in the NASA Icing Research Tunnel

Andy P. Broeren and Mark G. Potapczuk
Glenn Research Center, Cleveland, Ohio

Sam Lee
Vantage Partners, LLC, Brook Park, Ohio

Adam M. Malone and Bernard P. Paul, Jr.
Boeing Commercial Airplanes, Seattle, Washington

Brian S. Woodard
University of Illinois at Urbana-Champaign, Urbana, Illinois

Prepared for the
8th Atmospheric and Space Environments Conference
sponsored by the American Institute of Aeronautics and Astronautics
Washington D.C., June 13–17, 2016

National Aeronautics and
Space Administration

Glenn Research Center
Cleveland, Ohio 44135

September 2016

Acknowledgments

The authors wish to acknowledge the contributions of Colin Chen, a student in the NASA Icing Branch affiliated with Universities Space Research Association, who developed the Maximum Combined Cross Section algorithm and processed the 3-D scan data in support of this paper. The FAA and ONERA provided support for this work through interagency and international agreements, respectively. Specific contributions were made by the Universities of Illinois and Virginia under NASA Cooperative Agreement NNX12AB04A; the Boeing Company under Task Order NNC14TA36T; and by the University of Washington. The NASA-supported portion of this research was originally funded under the Atmospheric Environment Safety Technologies Project of the Aviation Safety Program with continued support under the Advanced Air Transport Technology and Aeronautics Evaluation and Test Capabilities Projects of the Advanced Air Vehicles Program. There were numerous individuals within each of these organizations that contributed to the design, development, fabrication, installation, testing of the hybrid models in addition to the post-test data analysis described in this paper. The successful and timely completion of this work could not have been accomplished without their dedicated contributions.

Level of Review: This material has been technically reviewed by technical management.

Ice-Accretion Test Results for Three Large-Scale Swept-Wing Models in the NASA Icing Research Tunnel

Andy P. Broeren and Mark G. Potapczuk
National Aeronautics and Space Administration
Glenn Research Center
Cleveland, Ohio 44135

Sam Lee
Vantage Partners, LLC
Brook Park, Ohio 44142

Adam M. Malone and Bernard P. Paul, Jr.
Boeing Commercial Airplanes
Seattle, Washington 98124

Brian S. Woodard
University of Illinois at Urbana-Champaign
Urbana, Illinois 61801

Abstract

Icing simulation tools and computational fluid dynamics codes are reaching levels of maturity such that they are being proposed by manufacturers for use in certification of aircraft for flight in icing conditions with increasingly less reliance on natural-icing flight testing and icing-wind-tunnel testing. Sufficient high-quality data to evaluate the performance of these tools is not currently available. The objective of this work was to generate a database of ice-accretion geometry that can be used for development and validation of icing simulation tools as well as for aerodynamic testing. Three large-scale swept wing models were built and tested at the NASA Glenn Icing Research Tunnel (IRT). The models represented the Inboard (20 percent semispan), Midspan (64 percent semispan) and Outboard stations (83 percent semispan) of a wing based upon a 65 percent scale version of the Common Research Model (CRM). The IRT models utilized a hybrid design that maintained the full-scale leading-edge geometry with a truncated afterbody and flap. The models were instrumented with surface pressure taps in order to acquire sufficient aerodynamic data to verify the hybrid model design capability to simulate the full-scale wing section. A series of ice-accretion tests were conducted over a range of total temperatures from –23.8 to –1.4 °C with all other conditions held constant. The results showed the changing ice-accretion morphology from rime ice at the colder temperatures to highly 3-D scallop ice in the range of –11.2 to –6.3 °C. Warmer temperatures generated highly 3-D ice accretion with glaze ice characteristics. The results indicated that the general scallop ice morphology was similar for all three models. Icing results were documented for limited parametric variations in angle of attack, drop size and cloud liquid-water content (LWC). The effect of velocity on ice accretion was documented for the Midspan and Outboard models for a limited number of test cases. The data suggest that there are morphological characteristics of glaze and scallop ice accretion on these swept-wing models that are dependent upon the velocity. This work has resulted in a large database of ice-accretion geometry on large-scale, swept-wing models.

I. Introduction

The modeling and simulation of ice-accretion formation on highly 3-D swept wings is an extremely complex problem that affects the design, certification and safe operation of transport airplanes. Broeren et al. (Ref. 1) describe the current situation where there is increasing demand to balance trade-offs in aircraft efficiency, cost and noise that tend to compete directly with allowable performance degradations over an increasing range of icing conditions. Icing simulation tools and computational fluid dynamics codes are reaching levels of maturity such that they are being proposed by manufacturers for use in certification of aircraft for flight in icing conditions. The large-scale proliferation of CFD tools is described in a recently released NASA report (Ref. 2) that outlines a research strategy to guide future CFD research. This report suggests that continued advancements in simulation technology should lead to airplane certification through analysis with significantly reduced or no reliance on traditional experimental approaches such as flight or wind-tunnel testing. This is a very ambitious and desirable goal, but will require significant long-term investments in research and development. In the specific case of icing simulation tools, there is currently no publically-available, high-quality, ice-accretion database to evaluate their performance for large-scale swept wings.

Swept-wing icing has been a significant research area of interest for many years. This work has mostly focused on icing physics studies that have been conducted to understand the physics of formation of ice accretion on swept wings and to develop models that allow their prediction (Refs. 3 to 14). This research has identified the unique features of swept-wing ice accretion such as the highly 3-D "scallop" or "lobster tail" formations that occur under certain conditions. The physical phenomena contributing to the formation of such features has been investigated with the development of accompanying analytical and empirical models with application to ice-growth prediction. This work has typically utilized small-scale symmetric models such as swept NACA 0012 wings or circular cylinders. While such models are appropriate for fundamental research, they are not representative in size, scale and section geometry to the swept wings of transport airplanes. This existing database might be useful to evaluate ice-prediction codes, but an additional database utilizing models of large-scale representative model geometry is required to increase confidence in ice-prediction codes such that they can be applied to the design and certification of modern transport airplanes.

The development of icing simulation tools has been documented over the years for codes such as LEWICE3D (Refs. 15 to 20), FENSAP-ICE (Refs. 21 and 22) and those developed by ONERA (Refs. 23 to 26) which predict particle trajectories and ice accretion for 3-D configurations. Some of these studies contain ice-accretion data acquired specifically for code development and evaluation, however the swept-wing geometries also tend to be smaller scale. Since swept-wing ice accretion under "scallop" or "lobster-tail" conditions is highly 3-D various "void fraction" or "ice density" approaches have been used in LEWICE3D to predict equivalent 2-D ice accretion cross-section geometries with much of the development data coming from a small-scale swept NACA 0012 wing (Ref. 20). In contrast to this, Szilder et al. (Refs. 27 and 28) have proposed a 3-D morphogenetic model that has shown the capability to capture the highly 3-D features associated with swept-wing ice accretion thus furthering the need for a representative database for which to evaluate their model.

In response to these challenges, NASA has partnered with the Federal Aviation Administration (FAA) and the Office National d'Etudes et Recherches Aérospatiales (ONERA) to sponsor a seven-phase, collaborative research effort into ice accretion characterization and its aerodynamic effect on large-scale swept wings. The sponsoring organizations are working with the Universities of Illinois, Virginia and Washington and the Boeing Company to achieve the overall goal of improving the fidelity of experimental and computational simulation tools for iced swept wings. Broeren et al. (Ref. 1) list the specific objectives of this research effort:

- Generate a database of 3-D, swept-wing, ice-accretion geometries for icing-code development and validation as well as for aerodynamic testing.
- Develop a systematic understanding of the aerodynamic effect of icing on swept wings including: Reynolds and Mach number effects, important flowfield physics and fundamental differences from 2-D.
- Determine the level of ice-shape geometric fidelity required for accurate aerodynamic simulation of swept-wing icing effects.

As these objectives imply, an important factor in evaluating the capability of icing simulation tools can be measured in terms of aerodynamic impact. For example, ice-accretion on swept wings is known to be highly 3-D under certain conditions. One aim of this research is to determine the extent to which this three-dimensionality affects the iced-wing aerodynamics relative to equivalent ice geometries that are more 2-D (i.e., little or no geometric variation in the spanwise direction). This research is a first step in understanding the impact of icing for a cruise-wing configuration without a wing-mounted engine. The resulting knowledgebase can then be used to extend the research to takeoff and landing configurations that are also important to design and certification of large commercial transport airplanes. Broeren et al. (Ref. 1) provide more detailed description of the research objectives and each of the seven research phases.

The objective of this present work is to provide an ice-accretion database for large-scale, swept-wing geometries suitable for icing-code evaluation and for follow-on aerodynamic studies. Three test campaigns were conducted in the NASA Icing Research Tunnel (IRT). Each campaign utilized a test article that represented a different spanwise station of a large-scale swept wing based upon the NASA Common Research Model (CRM) (Ref. 29). Aerodynamic data in the form of surface pressure and flow visualization were acquired for a range of angles of attack and flap deflections. The models were subjected to identical icing conditions that were scaled from typical in-flight icing scenarios for airplane missions representative of a large commercial transport. The resulting ice accretions were documented with photographs and 3-D quantitative measurements using a laser-based scanning method. This paper provides a description of the test-article design and development; the icing test matrix; a summary of the aerodynamic results; and a summary of the icing-test results.

II. Background: Model Selection and Hybrid Design

The CRM geometry was selected as the baseline model for this research because it is representative of current, modern design large commercial transport airplanes. In addition, all of the geometry is publically available and not export controlled. Therefore, there are no limitations to the distribution of the data from these experiments. The CRM was originally developed for the AIAA Drag Prediction Workshops and has also been used in subsequent experimental research efforts (Refs. 30 to 32). The fact that the CRM is representative of a wide-body transport airplane means that the physical size is very large compared to that of many other swept-wing airplanes such as single-aisle commercial transports including regional and business jets. The large physical size of the CRM wing presents specific challenges to the ice-accretion testing conducted in this project. Large-scale wing ice-accretion testing requires the design of “hybrid” or “truncated” models where the full-scale leading-edge geometry is matched to a shortened or truncated afterbody. The large physical size of the CRM wing requires a very aggressive design for the hybrid model that presents greater risk of adverse effects when installed in the NASA IRT. Therefore, the research team decided to use a 65 percent scale version of the CRM as the full-scale, baseline, reference geometry for this research. The CRM65 wing geometry, shown in Figure 1, compares favorably in size with existing single-aisle commercial transport airplanes. Using the CRM65 as the full-scale, baseline, reference geometry for this research reduces potential risks associated with the ice-accretion and aerodynamic testing while still being representative of current transport airplanes.

CRM65 Wing Geometry

- Semispan = 62.7 ft
- Root chord (symmetry plane) = 29.0 ft
- Root chord (fuselage side of body) = 25.4 ft
- Tip chord = 5.8 ft
- Mean aerodynamic chord = 15.0 ft
- Semispan area = 873 ft^2
- Aspect Ratio = 9.0
- Taper Ratio = 0.28
- Sweep angle ($c/4$) = 35 deg.

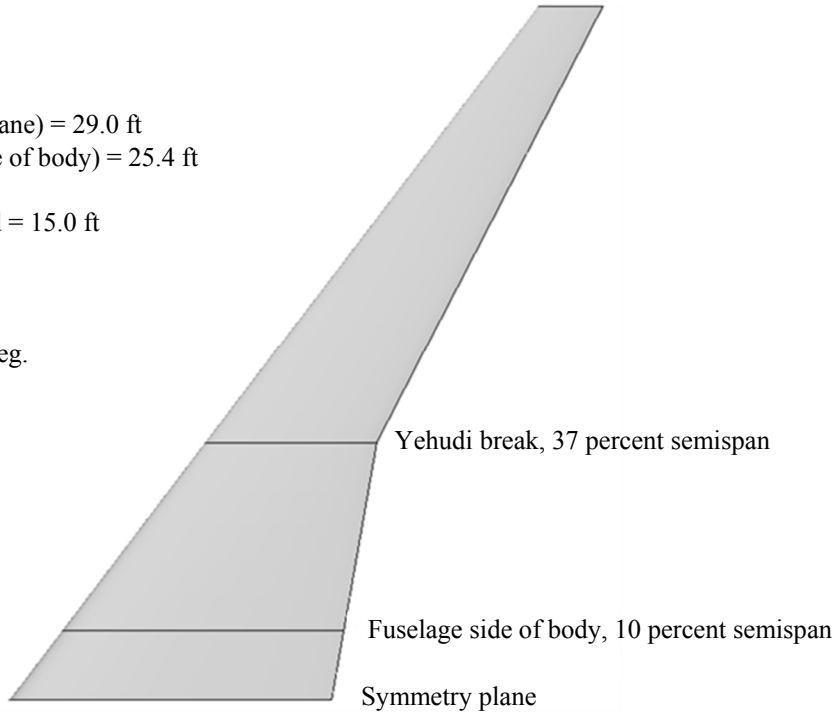

Figure 1.—Summary of CRM65 wing geometric characteristics, adapted from Broeren et al. (Ref. 1) and Vassberg et al. (Ref. 29).

The goal of the hybrid model design process was to combine the full-scale leading-edge geometry with a truncated aft section in order to reproduce the full-scale droplet impingement, leading-edge flow characteristics and resulting ice shape. References 33 to 38 describe the hybrid model design process used for this research with significant detail while a brief summary useful to the purposes of this paper is provided here.

This work was conducted under four main tasks:

- Selection of airplane mission and corresponding flight and icing conditions
- Simulation of the full-scale icing conditions
- Design and simulation of hybrid model wing sections in 2-D
- Design and simulation of hybrid model wing sections in 3-D

The approach in the first two tasks was to generate flowfield and ice-shape information in realistic flight and icing conditions. These results, such as the location of the attachment line along the wing, collection efficiency and ice-shape profiles then become the reference standard for the 2-D and 3-D hybrid model design studies carried out in the latter two tasks.

A set of icing mission scenarios was defined that were typical of large commercial transport airplanes and included climb, cruise, hold and descent phases of flight. The selection of airplane weights, flight speeds, altitudes and angles of attack for each flight phase was appropriate for an airplane of the CRM65 class. The selected icing conditions were based upon the Code of Federal Regulations Part 25 Appendix C continuous maximum envelope (App. C) and thus defined droplet MVD, cloud LWC and temperature.

The large matrix of flight and icing conditions was reviewed and a smaller number of cases were selected for further analysis. This subset of icing scenarios provided for a range of ice accretion on the full-scale airplane, while significantly reducing the workload associated with analyzing all cases. Flow simulations were performed at each of the selected flight conditions using the 3-D RANS code OVERFLOW (Ref. 39), thus generating a large database of flowfield information for the clean flight

baseline for the CRM65. The flowfield solution was used as input to the LEWICE3D ice-accretion prediction code to generate ice-shape results for the corresponding flight conditions.

A major outcome of this task was the selection of the spanwise locations to be used for the hybrid model designs for IRT testing. The section near the wing root, or inboard station, was selected to be at 20 percent semispan because this location corresponded to the minimum horn-ice angle for nearly all of the icing cases analyzed. The midspan station was selected to be at 64 percent semispan because this location corresponded to a change in the spanwise variation of the horn-ice angle for some of the icing cases analyzed. The section near the tip, or outboard station, was selected to be at 83 percent semispan. This location approximates the outboard extent of the wing leading-edge ice protection system in some cases, thus making the icing characteristics significant for that reason. This location is also about halfway between the 64 percent semispan station and the wing tip.

The design of hybrid models for icing tests where the full-scale leading-edge geometry is combined with a truncated afterbody has been explored by Saeed et al. (Refs. 40 to 42). Past research was conducted primarily for 2-D wing sections and for moderate model sizes that did not require special consideration of tunnel wall interference effects. In the current effort, these 2-D design methods were adapted to the swept-wing geometry and extended to include the effects of the tunnel walls on the large-blockage-model flowfield. A single-element slotted flap was also added to the hybrid model design at this stage. The flap was required to accommodate matching the leading-edge flow conditions (e.g., attachment line location) over the angle of attack range defined for the icing mission scenarios.

In simple infinite-swept wing theory, the flow at a spanwise wing station is approximated by the flow about the leading-edge-normal airfoil section at the appropriate 2-D Mach number and angle of attack. Since 2-D hybrid airfoil design methods are relatively well developed, the first step in the swept-wing wind-tunnel model design process took advantage of these 2-D tools to produce a representative 2-D hybrid airfoil. The 2-D hybrid airfoil sections were extended and swept to create the 3-D models. Consistent with infinite-swept-wing theory, these models had zero twist and zero taper greatly simplifying the design and ultimately, the construction of the models. In the IRT testing, each 3-D hybrid model was used to generate the ice accretion found at one spanwise station of the full-scale swept wing, which significantly simplified the hybrid model design process. A summary of the hybrid model design characteristics is shown in Table 1 for all three models. The hybrid and full-scale airfoil section coordinates are plotted in Figures 2 to 4. These plots show that each section included the local geometric angle of attack according to the wing twist distribution corresponding to airplane angle of attack equal to 0 deg. Therefore, only the airplane angle of attack needed to be specified to obtain the proper local angle of attack for each model.

The 3-D hybrid model designs were validated using 3-D simulation tools. This analysis included 3-D RANS flow simulations along with LEWICE3D icing simulations. The flow simulations were conducted to evaluate the effect of the test-section walls, the resulting flow separation and its impact on the hybrid model aerodynamics. The flow simulations were also used to optimize the flap deflection necessary to match the attachment line location to the clean flight baseline condition. With the proper flap deflection identified, the LEWICE3D simulations then provided droplet impingement and ice shape information for comparison to the iced flight baseline results generated earlier. The “acceptance criteria” for the final hybrid model design was based upon a number of comparisons. These comparisons were based purely on the results of 3-D RANS flowfield simulations and LEWICE3D icing simulations performed for both the CRM65 airplane flying the icing mission scenarios and the hybrid models designs “flying” in the IRT at the same conditions (e.g., airspeed, temperature, pressure, cloud MVD and LWC). Through the course of the research it was determined that it was important to match the attachment line location between the hybrid model in the IRT with the CRM65 in-flight baseline. In addition, the LEWICE3D-generated droplet impingement and ice shapes were also compared between the hybrid model in the IRT and the CRM65 in-flight baseline. The result of the hybrid model design process was the main element and flap “outer mold line” geometry for each of the three models: the Inboard model at 20 percent semispan; the Midspan model at 64 percent semispan and the Outboard model at 83 percent semispan.

TABLE 1.—IRT MODEL GEOMETRY INFORMATION

	Inboard	Midspan	Outboard
CRM65 Semispan Location	20%	64%	83%
Full-Scale (FS) Normal Chord, c_{FS} (in.)	297.9	122.7	91.3
Full-Scale (FS) Streamwise Chord (in.)	260.3	135.7	100.7
Upper-Surface FS Leading-Edge Extent (x/c_{FS})	0.04	0.10	0.17
Lower-Surface FS Leading-Edge Extent (x/c_{FS})	0.06	0.10	0.15
Model Scale Factor (c_{FS}/c_{Hyb})	2.25	2.0	1.5
Hybrid Model Normal Chord, c_{Hyb} (in.)	132.4	61.4	60.9
Hybrid Flap Normal Chord (in.)	32.7	15.1	15.0
Hybrid Model Streamwise Chord (in.)	161.8	74.6	74.0
Hybrid Flap Streamwise Chord (in.)	41.1	18.7	18.8
Upper-Surface FS Leading-Edge Extent Streamwise (in.)	15.0	15.4	19.5
Upper-Surface FS Removable Leading-Edge Extent Streamwise (in.)	11.2	12.3	11.4
Lower-Surface FS Leading-Edge Extent Streamwise (in.)	22.4	15.4	17.2
Lower-Surface FS Removable Leading-Edge Extent Streamwise (in.)	14.9	15.4	13.8

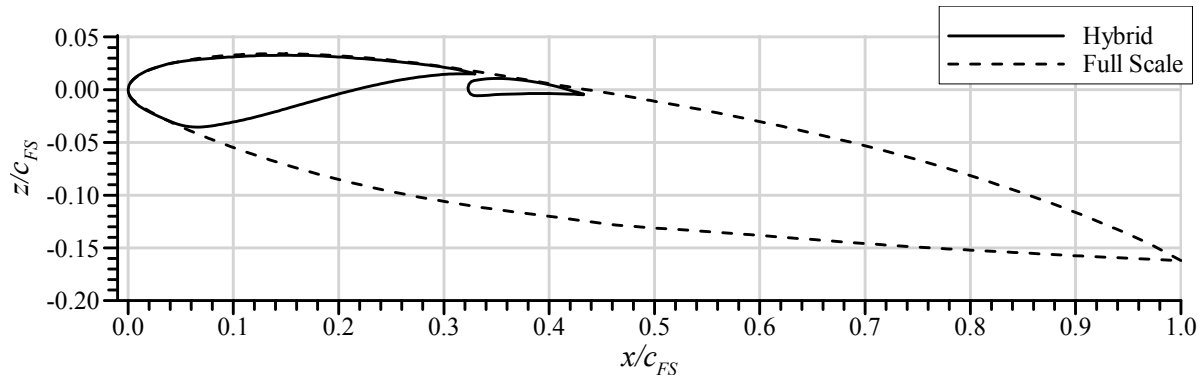

Figure 2.—Inboard model airfoil section (perpendicular to leading edge).

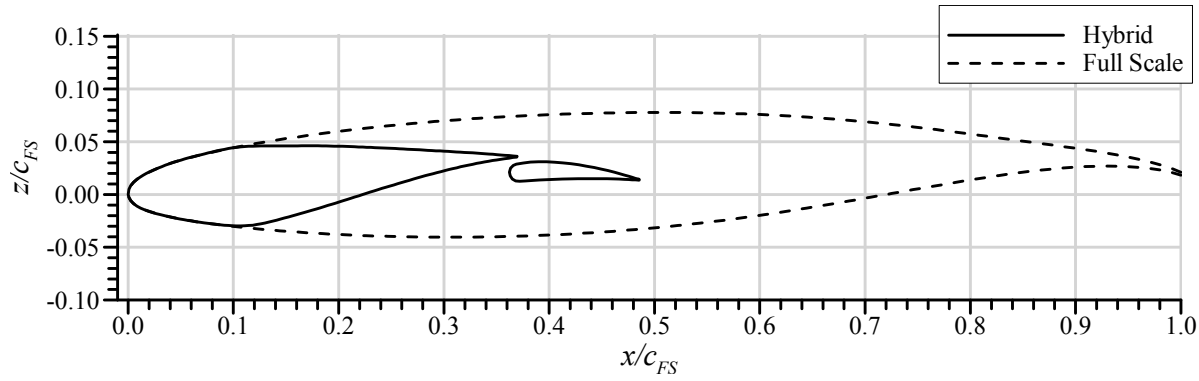

Figure 3.—Midspan model airfoil section (perpendicular to leading edge).

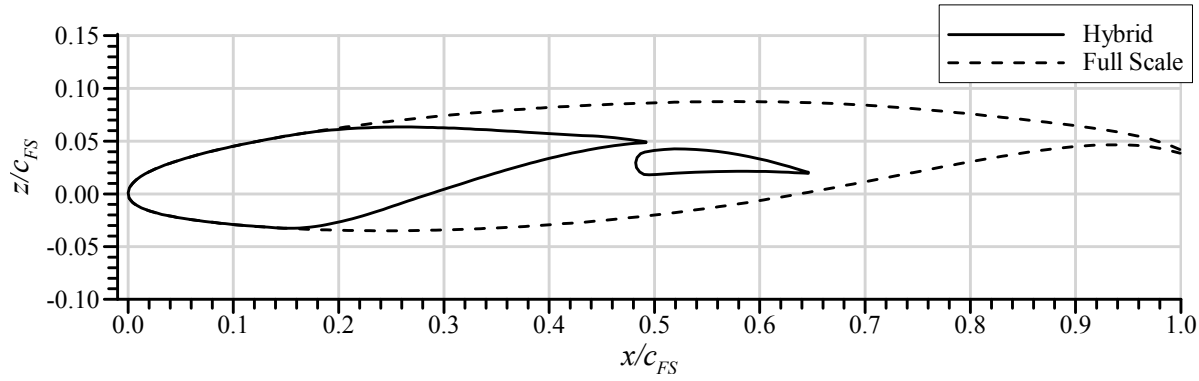

Figure 4.—Outboard model airfoil section (perpendicular to leading edge).

III. Wind-Tunnel Facility, Models and Experimental Methods

A. Wind-Tunnel Facility and Model

Ice-accretion testing was carried out at the NASA Glenn Icing Research Tunnel located in Cleveland, Ohio. The IRT is a closed-return, refrigerated wind tunnel that simulates flight through an icing cloud at pressure-altitudes near sea level. Temperature control is provided via an external refrigeration plant connected to a large heat exchanger that is located upstream of the settling chamber turning vanes. Downstream of the turning vanes are 10 rows of spray bars each with 55 possible nozzle positions. Two types of internal/external atomizing nozzles are available: Mod1 nozzles for lower water flow rates and Standard nozzles for higher water flow rates. Each nozzle set can be used independently or simultaneously depending upon the desired cloud conditions. The airflow and water droplets are accelerated to the test section via a 14-to-1 ratio contraction section. The test section is approximately 6 ft. high by 9 ft. wide by 20 ft. long and has a calibrated speed range from 50 to 325 knots (empty). The available temperature range is from –40 °C static to 20 °C total. The icing cloud is calibrated on a periodic basis and after any significant modification to the facility. Steen et al. (Ref. 43) describe the most recent calibration that was used for the present test campaigns. Soeder et al. (Ref. 44) provide a more detailed description of the facility.

Each model was mounted vertically in the test-section and spanned the entire height as shown in Figure 5. The model base plate was bolted to the turntable for angle of attack adjustment. Due to the large size of the models, the model base plate extended beyond the outer periphery of the turntable. Thus, there was a small gap of approximately 0.25 in. between the test-section floor and the model base plate. There was also a small gap of approximately 0.25 in. between the top of the model main element and the test-section ceiling. The model was also supported at the ceiling interface with a 1.0 in. diameter pin located at the model center of rotation. The gaps between the model and the floor and ceiling were significantly larger for the flap to accommodate flap angles from 0 to 30 deg.

Each model was comprised of a main element, single-element slotted flap and removable leading-edge section. Some details of the model geometries are shown in Table 1 including the upper and lower surface extents of the full-scale leading edge. The main element and flap were instrumented with three streamwise rows of surface pressure taps that were located at spanwise stations 18, 36, and 54 in. above the test-section floor. Three thermocouples were installed inside the main element structure and these temperatures were monitored to ensure that the model temperature was in equilibrium with the surrounding air. There were two different interchangeable leading edges for each model. One leading edge was used for surface-pressure measurements and was instrumented with pressure taps in three streamwise rows corresponding to the spanwise stations on the main element and flap. The other leading edge was used for icing tests and thus has a completely smooth exterior surface. The removable leading edges were made from 0.090 in. thick aluminum that was stretch-formed to the desired airfoil coordinates and then hard anodized to improve the surface durability. For the icing leading edge, five thermocouples

Figure 5.—Pictures of each model installed in the IRT test-section; from left to right: Inboard model, Midspan model and Outboard model.

were located on the inside surface of the skin. Commercially available electrothermal heaters were also mounted to the inside surface of the icing leading edge. These heaters were only used to deice the leading edge after the ice accretion was fully documented.

The flap of each model had a motorized drive system with positioning feedback provided via a calibrated linear potentiometer. The flap control switch was located in the control room with the flap angle readout on the IRT Escort data system. The flap was also equipped with a custom-designed, anti-icing, electrothermal surface heater. It was important to the hybrid design that the flap aerodynamics not be compromised by any ice accretion. The heaters were connected to the IRT's California Instruments MX-45 power supply. The power supply was energized from the control room prior to the initiation of the icing spray. Twelve thermocouples were installed in various locations beneath the flap heater to monitor the skin temperature.

B. Experimental Methods

The models were tested in three separate test campaigns. The Midspan model was also utilized for a brief two-day test campaign approximately five months later. Each model was initially installed in the IRT test section with the pressure-instrumented leading edge. The model surface pressures were measured over a large range of angle of attack and flap deflections in order to track the location of the attachment line at the spanwise station 36 in. above the test-section floor (model centerline). At the conclusion of these aerodynamic tests, the pressure-instrumented leading edge was removed and the icing leading edge was installed. For icing tests, the desired temperature and speed conditions were established with the appropriate time allotted for the model and tunnel to thermally equilibrate. The icing spray cloud was turned on for the desired period of time and then the tunnel was shut down to allow for documentation of the ice accretion. Photographs were taken first, followed by 3-D digital measurement using a laser-based scanning system (Refs. 45 to 47). In some cases, a section of the ice was removed from the model and weighed after the 3-D measurements were completed.

The ice accretion results shown in this paper consist of 2-D section cuts and photographs to document the general 3-D morphology. Many of the ice accretions observed during the IRT test campaigns were highly 3-D, such that any type of 2-D description is limited. Given that icing simulation tools typically provide 2-D ice-shape cross-sections, results of this type are required for comparison. The approach that was used for this paper was to take 30 section cuts through the 3-D scan of the ice accretion perpendicular to the wing leading edge as shown in Figure 6. These 30 section cuts were taken at a spacing of 0.2 in.,

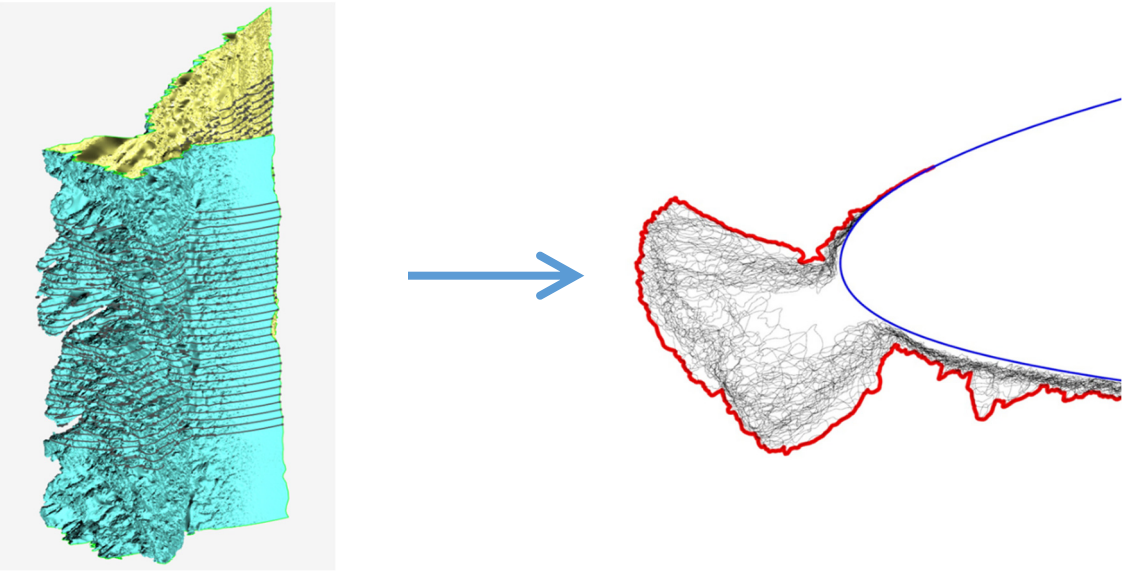

Figure 6.—Schematic description of process used to determine Maximum Combined Cross-Section (MCCS) of the 3-D ice accretion.

thus covering 6 in. of ice accretion along the leading edge near the model centerline, 36 in. above the floor. The section cuts were projected onto a single plane and the maximum outer boundary was obtained. The resulting Maximum Combined Cross Section, or MCCS, represents the outermost extent of the ice over that 6-in. segment. The 6-in. segment was determined to be sufficient to capture all of the significant features of the ice accretions in these test campaigns. The MCCS is considered to be equivalent to the traditional hand-tracing method that typically results in the maximum outer boundary of an ice accretion. Traditionally, digitized hand tracings of ice accretion have been the basis for evaluation of icing simulation codes such as LEWICE3D.

All model and facility data were recorded on the IRT Escort D data system (Ref. 44). The model data included the surface pressures, thermocouple temperatures and flap angle potentiometer described in the previous paragraphs. The facility data included the aerodynamic flow conditions, icing cloud parameters from the spray bars and temperatures. During the ice-accretion runs, these data were acquired at a rate of one measurement per second or one measurement per 10 sec depending upon the duration of the icing spray. The data acquisition was automatically triggered with the initiation of the spray and concluded with termination of the spray. The model surface pressure data were acquired with an Electronically Scanned Pressure (ESP) system. Each pressure tap was connected to an available port on a 5 psid ESP module. The pressure coefficient was calculated using the average static and differential pressures measured on the North and South Pitot-static probes in the bellmouth. No correction or test-section calibration was applied to these pressures.

In addition to these measurements, surface oil flow visualization was also performed for the Inboard and Midspan models in the dry, or un-iced, configuration. The flow visualization was used to identify any regions of significant flow separation that was an important concern during the hybrid model design phase. The upper surface of the main element and flap was covered in flat-black, self-adhesive contact paper. The contact paper provided a smooth background surface with uniform color that greatly improved the flow visualization images. A light coat of motor oil was then applied to the upper surface. Automotive type fluorescent dye was added to mineral oil and applied to the model with sponge rollers. After a uniform covering of the dyed oil was achieved, the model was set to the desired incidence and flap angles. The tunnel was started and run at the desired speed for 2 to 3 min to allow the surface oil to reach a time-averaged pattern. After the tunnel was stopped, photographs were taken under UV-black light illumination.

C. Aerodynamic and Icing Test Conditions

The aerodynamic and icing test conditions were based upon the in-flight icing mission scenarios for the CRM65 airplane originally used in the hybrid model design process as described in Section II. There were at least seven different mission scenarios that were considered during the model design phase. In planning for the IRT test campaigns, three of these scenarios were selected as the reference conditions and are summarized in Table 2. All of the cases are for the airplane configured with flaps up which is consistent with the existing CRM65 geometry used for this work. The WB33 and WB41 cases are holding conditions in App. C continuous maximum icing. The WB33 case was a low gross weight (LGW) condition. The WB41 case had a slightly higher angle of attack and lower speed due to the high gross weight (HGW). The WB52 case is a descent condition and thus had a lower angle of attack and significantly reduced exposure time to the icing conditions.

A key advantage and motivation behind the hybrid model design approach utilized in this effort was maintaining the full-scale wing leading-edge geometry in order to generate flight-scale representative ice accretion. However, the resulting model sizes were still large relative to the IRT test section. These large model sizes, particularly for the Inboard model, limited the maximum speed that could be obtained. This limitation was primarily due to the solid and wake blockage effects of the model in addition to high aerodynamic loads. Prior to the conduct of the testing, it was recognized that the speeds shown in Table 2 were most likely unrealistic, particularly for the Inboard model. Therefore, this model was tested in the first campaign and it was found that the optimum speed for icing tests was 130 knots for each case shown in Table 2. The maximum obtainable speeds were slightly higher, particularly for the WB52 case since

TABLE 2.—SUMMARY OF FLIGHT REFERENCE ICING CONDITIONS

Case	Flight phase	Weight	Angle of attack, deg.	Static pres., KPa	Mach	TAS, knots	Total temp., °C	Static temp., °C	MVD, μm	LWC, g/m^3	Exposure time, min.
WB33 T-4	Hold	LGW	3.7	69.7	0.36	232	3.2	–4.0	20	0.55	45.0
WB33 T-6	Hold	LGW	3.7	69.7	0.36	231	1.1	–6.0	20	0.51	45.0
WB33 T-13	Hold	LGW	3.7	69.7	0.36	228	–6.1	–13.0	20	0.36	45.0
WB33 T-25	Hold	LGW	3.7	69.7	0.36	223	–18.4	–25.0	20	0.17	45.0
WB41 T-6	Hold	HGW	4.4	84.3	0.35	225	0.6	–6.0	20	0.51	45.0
WB41 T-13	Hold	HGW	4.4	84.3	0.35	222	–6.6	–13.0	20	0.36	45.0
WB41 T-25	Hold	HGW	4.4	84.3	0.35	217	–18.9	–25.0	20	0.17	45.0
WB52 T-6	Descent	Nominal	2.1	84.3	0.41	263	3.1	–6.0	20	0.51	4.0
WB52 T-13	Descent	Nominal	2.1	84.3	0.41	259	–4.1	–13.0	20	0.36	4.0
WB52 T-25	Descent	Nominal	2.1	84.3	0.41	253	–16.5	–25.0	20	0.17	4.1

this had the lowest angle of attack. It was determined that some margin on fan power was required and that running all three cases at the same speed was a useful simplification. Since a key objective of this work was to simulate the ice accretion that would build up on the CRM65 airplane wing, identical icing conditions including the speed of 130 knots were used for all three models. A limited set of conditions at higher speeds were also performed for the Midspan and Outboard models since these models could achieve the speeds shown in Table 2.

The reference cases listed in Table 2 along with the speed limitation of 130 knots required modifications to the aerodynamic and icing conditions for the IRT tests. Further simplifications to the matrix were also performed in order to generate ice accretion that was more readily suited to icing-code evaluation. For example, the WB33 conditions in Table 2 reflect a change in the reference speed, temperature and cloud LWC according to App. C. While this is appropriate for airplane certification icing analysis, the changes to multiple variables complicated the use of the resulting ice accretion for icing-code evaluation. It was considered more useful to hold constant all other variables and vary the temperature over a desired range. Therefore, most of the IRT test conditions depart from the App. C envelope used for icing certification. In order to account for the reduction in speed to 130 knots, a scaling analysis was performed to match the freezing fraction at the attachment point and the product of the local collection efficiency at the attachment point and the accumulation parameter. These are standard scaling methods that have been developed primarily for model-size scaling applications (Ref. 48).

The resulting IRT test conditions are shown in Table 3. Run ID 1 through 8 reflect the variation in temperature with all other conditions held constant. The 29 min exposure time for these cases resulted from an approximate scaling of the 45 min exposure shown for the WB33 T-13 flight reference case in Table 2. Run ID 9 in Table 3 resulted from a direct scaling of the WB33 T-25 flight reference case in Table 2. Run ID 10, 11, and 11.1 were short-duration exposures designed to look at ice roughness characteristics in the early stages of ice build-up. Run ID 12 and 13 were included to explore the effect of larger drop sizes on the ice accretion characteristics. Run ID 14 and 15 were scaled equivalents to Run ID 4 with a smaller drop size. Run ID 18 was identical to Run ID 4, but at the WB41 angle of attack = 4.4 deg. Run ID 21 and 22 were identical to Run ID 3 and 4, but at the WB52 angle of attack = 2.1 deg. Run ID 23 was scaled directly from the WB33 T-6 case in Table 2. The remaining conditions were only run on the Midspan or Outboard models and were included to evaluate effects of airspeed and model incidence. In addition to the conditions listed in Table 3, numerous repeat runs were performed for each of the three models. Ice-accretion repeatability was verified during the test campaigns by performing a direct comparison of the 3-D scan data.

TABLE 3.—SUMMARY OF IRT TEST CONDITIONS FOR THE RESULTS IN THIS PAPER

Run ID	Angle of attack, deg.	Inboard flap, deg.	Midspan flap, deg.	Outboard flap, deg.	TAS, knots	Total temp., °C	Static temp., °C	MVD, μm	LWC, g/m^3	Exposure time, min
1	3.7	13.7	25.0	14.0	130	1.0	–1.2	25	1.00	29.0
2	3.7	13.7	25.0	14.0	130	–1.4	–3.6	25	1.00	29.0
3	3.7	13.7	25.0	14.0	130	–3.8	–6.0	25	1.00	29.0
4	3.7	13.7	25.0	14.0	130	–6.3	–8.5	25	1.00	29.0
5	3.7	13.7	25.0	14.0	130	–8.7	–11.0	25	1.00	29.0
6	3.7	13.7	25.0	14.0	130	–11.2	–13.5	25	1.00	29.0
7	3.7	13.7	25.0	14.0	130	–15.0	–17.2	25	1.00	29.0
8	3.7	13.7	25.0	14.0	130	–23.8	–26.0	25	1.00	29.0
9	3.7	13.7	25.0	14.0	130	–17.9	–20.1	25	0.60	23.0
10	3.7	13.7	25.0	14.0	130	–17.9	–20.1	25	0.60	2.5
11	3.7	13.7	25.0	14.0	130	–1.4	–3.6	25	1.00	2.5
11.1	3.7	13.7	25.0	14.0	130	–6.3	–8.5	25	1.00	2.5
12	3.7	13.7	25.0	14.0	130	–20.0	–22.2	35	0.60	24.0
13	3.7	13.7	25.0	14.0	130	–20.0	–22.2	35	0.60	2.5
14	3.7	13.7	25.0	14.0	130	–6.7	–8.9	20	1.40	26.5
15	3.7	13.7	25.0	14.0	130	–4.9	–7.2	20	1.00	37.4
18	4.4	13.7	28.0	17.0	130	–6.3	–8.5	25	1.00	25.5
21	2.1	13.7	14.0	9.0	130	–3.8	–6.0	25	1.00	29.0
22	2.1	13.7	14.0	9.0	130	–6.3	–8.5	25	1.00	29.0
23	3.7	13.7	25.0	14.0	130	–3.1	–5.3	27	0.91	45.0
23.1	3.7	N/A	25.0	N/A	130	–3.1	–5.3	27	0.91	32.0
30	3.7	N/A	N/A	14.0	232	–11.2	–18.3	20	0.30	25.3
31	7.5	N/A	0.0	N/A	130	–6.3	–8.5	25	1.00	29.0
32	3.7	N/A	25.0	N/A	180	–2.0	–6.3	24	0.65	32.0
34	2.1	N/A	N/A	9.0	247	1.2	–6.8	22	0.38	30.0

IV. Results and Discussion

A. Aerodynamic Calibration Results

Surface pressure data were acquired for each of the three hybrid models prior to the start of the icing tests. The pressure data acquired on the leading edge at the 36 in. station (model centerline) were used to track the location of the attachment point as a function of the model incidence and flap angles. The attachment point was defined as the location of maximum pressure coefficient. The aim of the aerodynamic calibration was to match the attachment point location on the IRT model to the attachment point location on the CRM65 wing at the corresponding spanwise location. These locations were determined from analysis of the clean flight baseline CFD simulations described in Section II and were expressed in terms of the surface wrap distance measured from the forward-most leading-edge location or "hilite." Table 4 provides a summary of these locations as originally determined for the flight cases identified in Table 2. Note that in this paper, the surface wrap distances are given as positive values along the airfoil lower surface. The attachment point locations in the following aerodynamic calibration plots are approximations of the true location of the maximum pressure coefficient because the locations were determined by visual inspection of the C_p data plotted in real-time during the test runs. This method was used in lieu of a quantitative analysis of the pressure data to save time during the test. The visual inspection method was determined to be effective for providing the map of the attachment point location as a function of incidence and flap angle. Pressure data were acquired and stored for each point such that a post-test analysis could be performed later, as needed. It is highly likely that the attachment point locations shown in Figures 7, 9, and 11 would be slightly modified based upon a quantitative analysis. However, the general trends would most certainly remain unchanged. The locations in Table 4 were updated after further analysis of the clean flight baseline CFD simulations that was conducted after the IRT test campaigns. This analysis led to a more precise definition of the leading-edge hilite location, thus changing the wrap distance to the attachment point. The updated locations, shown in Table 5 were closer to the hilite in most cases. The effect of this is described in the following discussion.

TABLE 4.—ORIGINAL ATTACHMENT POINT LOCATIONS

		Streamwise wrap distance from hilite[a]		
Reference case	Angle of attack, deg.	Inboard model, in.	Midspan model, in.	Outboard model, in.
WB33	3.7	4.72	1.66	1.06
WB41	4.4	5.28	1.91	1.42
WB52	2.1	2.85	0.57	0.36

[a]Note that the wrap distances are positive on the lower surface.

TABLE 5.—UPDATED ATTACHMENT POINT LOCATIONS

		Streamwise wrap distance from hilite[a]		
Reference case	Angle of attack, deg.	Inboard model, in.	Midspan model, in.	Outboard model, in.
WB33	3.7	4.32	1.34	0.85
WB41	4.4	4.81	1.76	1.15
WB52	2.1	3.00	0.61	0.33

[a]Note that the wrap distances are positive on the lower surface.

The aerodynamic calibration for the Inboard model is shown in Figure 7. These data were acquired at a speed of 100 knots because the high incidence and flaps angles increased the aerodynamic loads and blockage thereby requiring a lower speed. Data were acquired at incidence angles of 1, 3, and 5 deg. for flap angles of 0, 5, 10, and 15 deg. with an additional point at 6 deg. incidence for flap angle = 0 deg. The plot shows that the attachment point location moved downstream from the hilite (increasing wrap distance) with increasing incidence and flap angles. Also shown in Figure 7 are the desired attachment point locations from Table 4 that were derived from the CRM65 airplane CFD simulations. For example, the WB33 case attachment point was located at a distance of 4.72 in. from the hilite. The data in Figure 7 show that this location could be achieved by setting the model to an angle of attack of 3.5 deg. with a flap angle close to 15 deg., or an angle of attack of 5.7 deg. with a flap angle close to 0 deg. These combinations would provide matching of the attachment point location on the IRT model to that of the corresponding flight condition. However, it was determined prior to the test that the best choice for angle of attack was the flight reference angle of attack shown in Table 2 which was 3.7 deg. for the WB33 case. Referring back to Figure 7, a flap angle between 10 and 15 deg. was required to produce the desired attachment point location for $\alpha = 3.7$ deg.

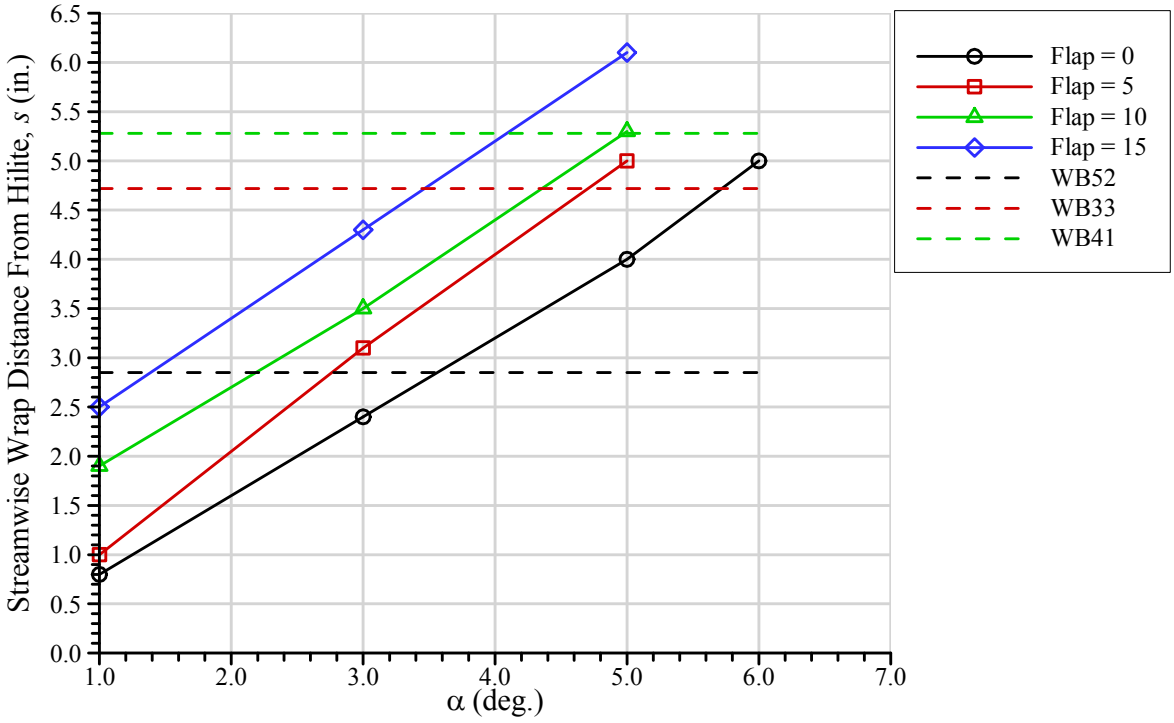

Figure 7.—Approximate attachment point location on Inboard model as a function of model incidence and flap angles. Data were acquired at 100 knots and total temperature = 10.8 °C.

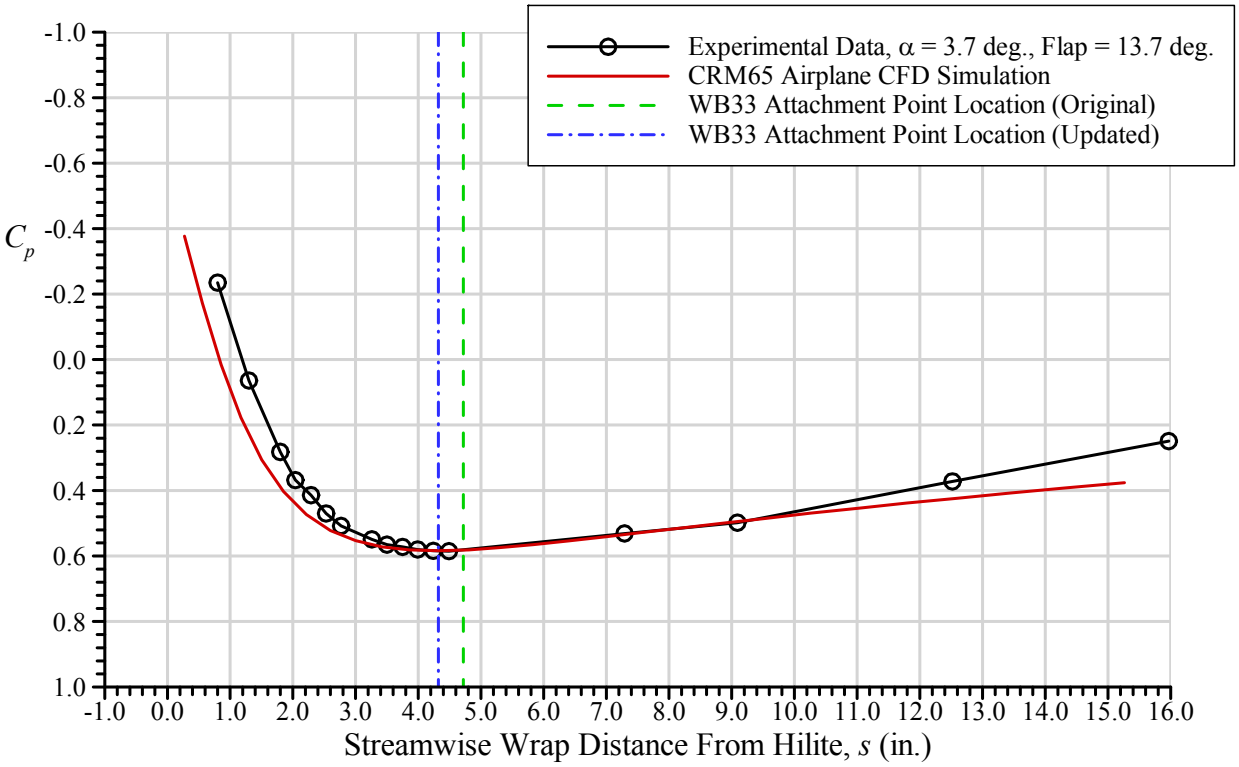

Figure 8.—Inboard model pressure distribution plotted against streamwise wrap distance near the attachment point. Data were acquired at 140 knots and total temperature = –11.9 °C.

This information was utilized in an iterative search for the correct flap angle required to produce the WB33 attachment point location for α = 3.7 deg. The flap angle was subsequently adjusted in small increments with pressure data acquired at each angle to produce the best matching of attachment point location. The optimal flap angle was determined to be 13.7 deg. Figure 8 shows the pressure coefficient on the wing leading edge in the region of the attachment point for this flap angle. The C_p data are plotted against the wrap distance along with the original WB33 location at s = 4.72 in. and the updated WB33 location at s = 4.32 in. Provided for comparison is the corresponding leading-edge pressure distribution that was extracted from the clean flight baseline CFD simulation. This plot confirms that the updated attachment point (s = 4.32 in.) coincides with the maximum C_p for the CRM65 airplane CFD simulation. The comparison of the experimental pressure data with the CFD simulation results is only valid in the region of the attachment point according to hybrid model design procedure. These pressure data would not be expected to compare well outside of this region because of the significant differences between the hybrid IRT model versus the full 3-D airplane.

The maximum C_p in the experimental data lies between the original and updated WB33 locations. Thus a slightly lower flap angle would be required to match the updated attachment point location corresponding to the WB33 reference case in Table 5. The flap angle of 13.7 deg. was higher than the flap angle of 6 deg. that was determined during the hybrid model design process (Refs. 35 and 38) using 3-D CFD tools and is a measure of the uncertainty in the CFD prediction of the hybrid model performance in the IRT.

A similar procedure was followed for the WB52 and WB41 cases where the desired angles of attack were 2.1 and 4.4 deg., respectively (cf. Table 2). As indicated in the aerodynamic calibration plot (cf. Fig. 7) the corresponding flap angles were also between 10 and 15 deg. The flap angle of 13.7 deg. was also found to be optimal for both WB52 and WB44 cases in addition to the WB33 case.

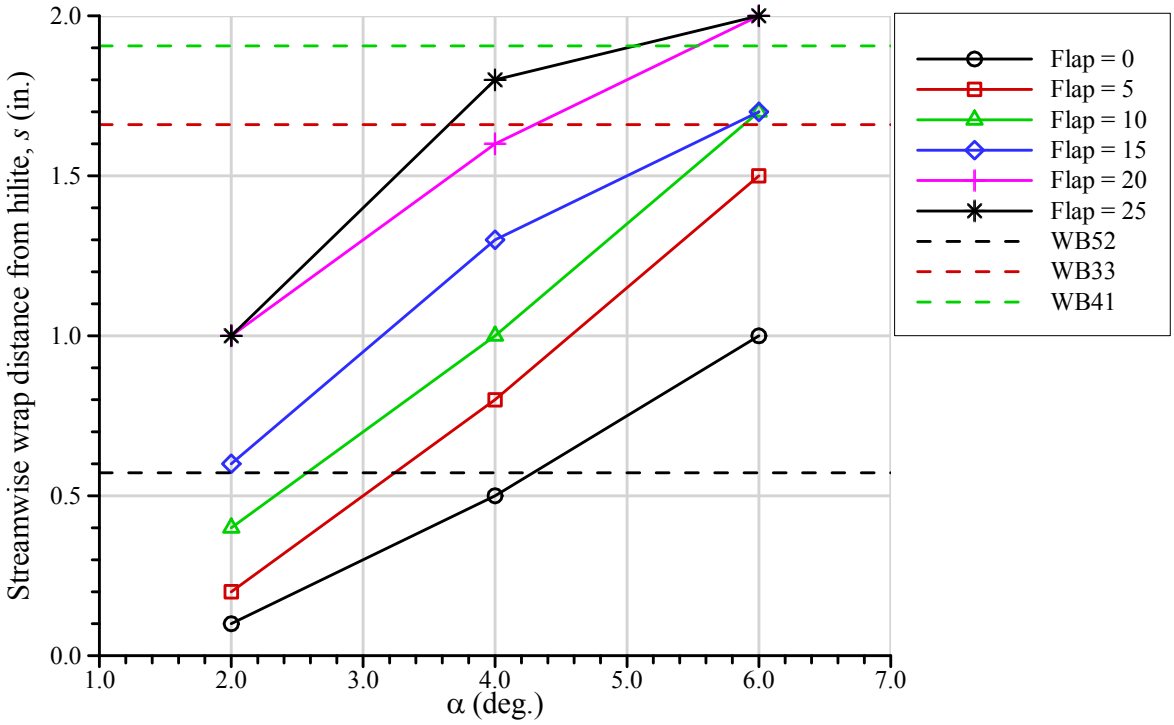

Figure 9.—Approximate attachment point location on Midspan model as a function of model incidence and flap angles. Data were acquired at 130 knots and total temperature = –9.2 °C.

The aerodynamic calibration plot for the Midspan model is shown in Figure 9. These data were acquired at a speed of 130 knots, angles of attack of 2, 4 and 6 deg. and flap angles of 0, 5, 10, 15, 20, and 25 deg. The significantly smaller size of the Midspan model relative to the Inboard model allowed for the higher speed and flap angles. As Figure 9 indicates, the larger flap angles were needed to match the attachment point locations at the flight reference angles of attack for the WB33 (α = 3.7 deg.) and WB41 (α = 4.4 deg.) cases. Following a similar procedure that was used for the Inboard model, the flap angle was adjusted in small increments between two positions to optimize the matching of the attachment point location. For the WB52 case with α = 2.1 deg. the flap angle was varied between 10 and 15 deg., with 14 deg. being identified as providing the best match in the attachment point location. For the WB33 case with α = 3.7 deg., the flap angle was varied between 20 and 25 deg. with 25 deg. being identified as the best match. Finally, for the WB41 case with α = 4.4 deg. the best match was determined to be at a flap angle of 28 deg. Surface pressure data were acquired for these configurations both at a speed of 130 knots and also at a higher speed in the range of 230 to 260 knots. These data were used to verify that the location of maximum pressure did not change at the higher speed (i.e., higher Reynolds and Mach number) condition.

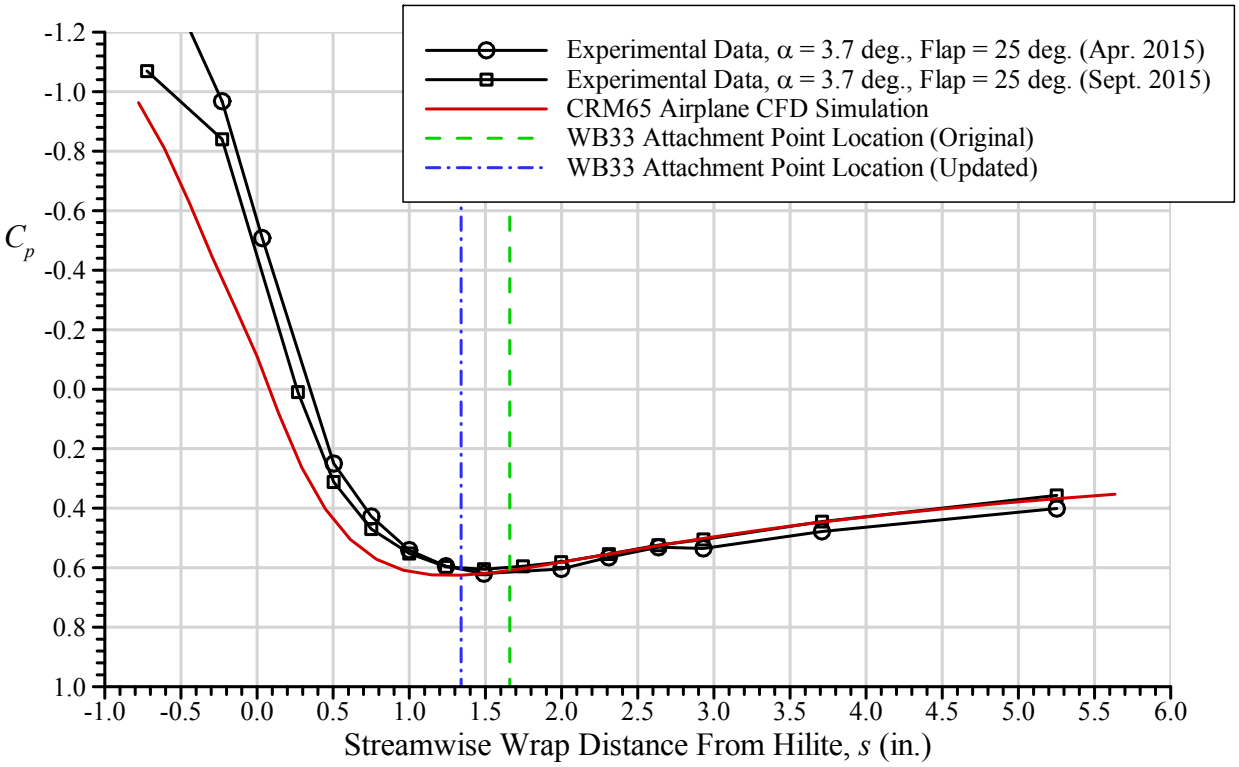

Figure 10.—Midspan model pressure distribution plotted against streamwise wrap distance near the attachment point. Data were acquired at 130 knots and total temperature = –9.2 °C.

Leading-edge pressure data for the WB33 case are shown in Figure 10 for the Midspan model along with a comparison to the airplane CFD simulation. Two sets of experimental data are shown in Figure 10. The original data set is from April 2015 along with a repeat set of data acquired in September 2015 during a short test campaign with this model. While there are some differences in the measured pressure coefficients, the location of minimum pressure is well matched between the two sets of experimental data. The experimental data indicate that the maximum C_p was at s = 1.5 in., in between the original and updated WB33 target locations. Based upon the aerodynamic calibration data in Figure 9, a lower flap angle less than 20 deg. would be required to match the updated attachment point location. Reducing the flap angle to less than 20 deg. would still likely be higher than the 15 deg. that was determined during the hybrid model design process (Refs. 35 and 38) using 3-D CFD tools and is a measure of the uncertainty in the CFD prediction of the hybrid model performance in the IRT.

The aerodynamic calibration plot for the Outboard model is shown in Figure 11. These data were gathered at the same speed, incidence and flap angles used for the Midspan model. The plot shows that significantly lower flap angles were required on the Outboard model to match the desired attachment point locations. For example, the WB33 case at α = 3.7 deg. required a flap angle between 10 and 15 deg., with the best match occurring at 14 deg. determined through the iterative search procedure. For the WB52 case at α = 2.1 deg., the best match occurred with a flap angle of 9 deg. For the WB41 case at α = 4.4 deg., the best match occurred with a flap angle of 17 deg. Figure 12 shows the attachment region pressure coefficient for the WB33 case along with the corresponding airplane CFD simulation result. The experimental data indicate that the location of maximum C_p was near s = 1.0 in., in between the original and updated WB33 target locations. Based upon the aerodynamic calibration data in Figure 11, a lower flap angle less than 10 deg. would be required to match the updated attachment point location. Surface pressure data were also acquired for these configuration at higher speeds in the range of 230 to 260 knots as was performed for the Midspan model.

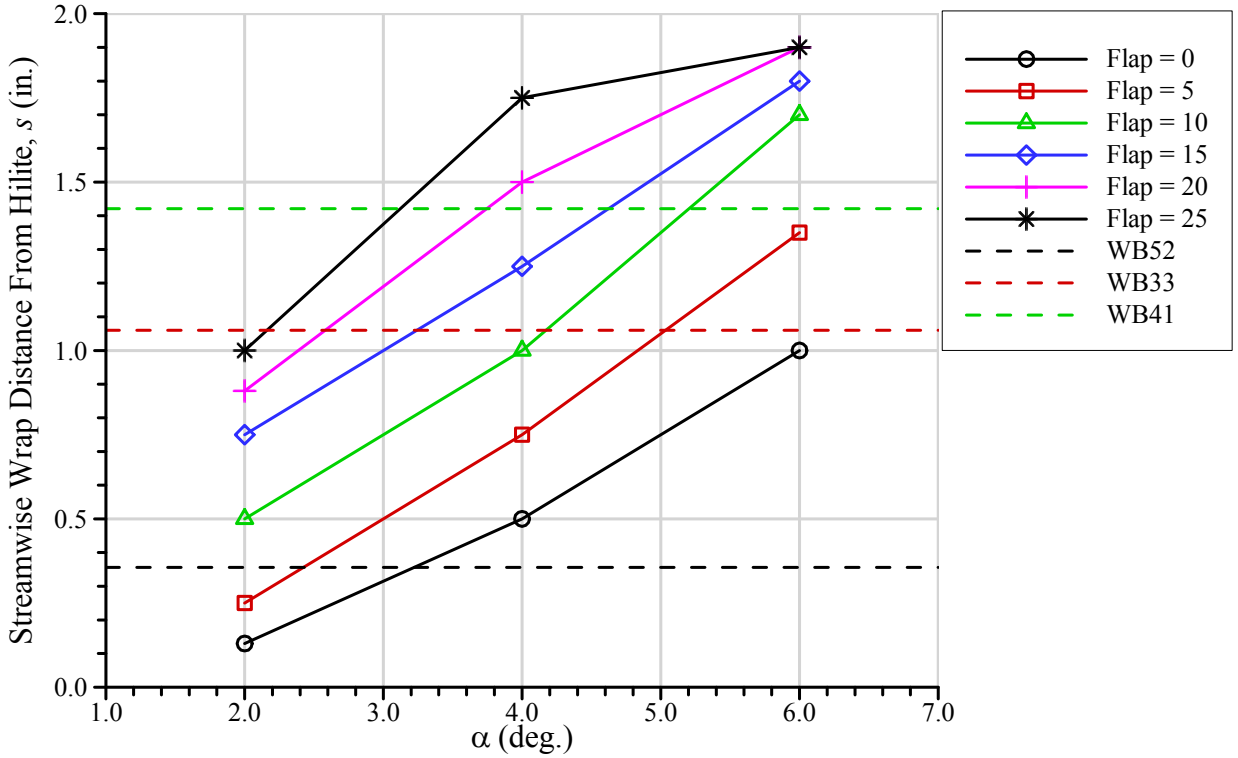

Figure 11.—Approximate attachment point location on Outboard model as a function of model incidence and flap angles. Data were acquired at 130 knots and total temperature = 11.0 °C.

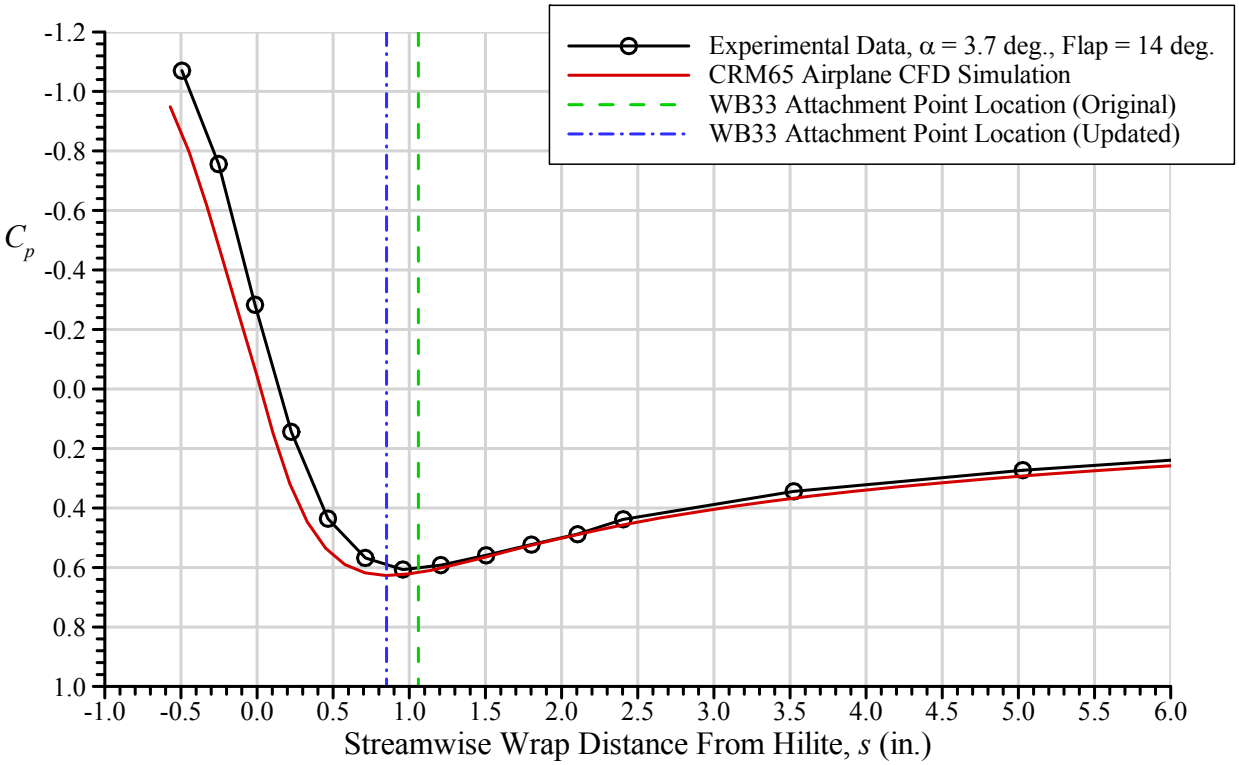

Figure 12.—Outboard model pressure distribution plotted against streamwise wrap distance near the attachment point. Data were acquired at 130 knots and total temperature = 11.0 °C.

B. Surface-Pressure Results

During the aerodynamic calibration process, pressure data were acquired for all three pressure tap rows on the main element and flap of each model. Figure 13 shows these pressures for the Inboard model at the WB33 configuration ($\alpha = 3.7$ deg., Flap = 13.7 deg.). The x-location for the pressures are shown in inches relative to the model center of rotation in the IRT. The y-location is measured relative to the IRT test-section floor with $y = 36$ in. corresponding to the model centerline. Since the leading edge of the model is swept back from the floor ($y = 0$ in.) to the ceiling ($y = 72$ in.), the x-locations increase with y-location. The data show the increasing suction pressure on the leading edge working from $y = 18$ in. outboard to $y = 54$ in. This is consistent with the spanwise variation in lift on the model from the floor to the ceiling due to the spanwise flow. On the lower surface, there was a distinct slope change in the pressure distribution owing to the transition from the full-scale leading-edge geometry to the truncated aft section. For example, this slope change occurred at $x \approx -45$ in. for the pressure data at $y = 36$ in. The corresponding change in geometry can be seen in Figure 2 at $x/c_{FS} \approx 0.06$. The pressures measured on the flap indicated little or no flow separation with the C_p values converging to a near-zero value at the trailing edge.

Similar data are shown for the Midspan model in Figure 14. These pressure profiles exhibit a slope change on the lower surface (e.g., at $x \approx -20$ in. for $y = 36$ in.) that can be attributed to the transition from the full-scale leading-edge geometry to the truncated aft section. This change in geometry can be seen in Figure 3 at $x/c_{FS} \approx 0.12$. There were also slope changes on the upper surface, such as at $x \approx -25$ in. and -20 in. for $y = 36$ in. The changes in the pressure distribution were attributed to variations in the airfoil model surface coordinates resulting from the hybrid design process and transition from the full-scale leading edge to the truncated aft section. The pressures measured on the flap indicated relatively high values of suction pressure due to the large flap angle of 25 deg. These pressures also indicate a full recovery to near zero values of C_p at the trailing edge suggesting little or no flow separation on the flap. Also shown in Figure 15 is a comparison of the surface pressure measured in September 2015 for the $y = 36$ in. station. This comparison is complicated by the fact that some pressure taps were removed from the measurements for each data set. For example, there were two pressure taps removed from the flap leading edge for the September 2015 data compared to April 2015. The functionality of these taps was lost between April and September 2015. Aside from these issues, the overall agreement is acceptable.

The surface pressure data for the Outboard model are shown in Figure 16. The pressure profiles exhibited similar characteristics to the Midspan and Inboard models. The slope changes on the upper surface were significantly smaller than for the Midspan model reflecting improvements in the hybrid model design process as the Outboard model was designed after the Midspan and Outboard models. The pressures measured on the flap indicated full recovery to near zero values of C_p at the trailing edge suggesting little or no flow separation which is consistent with that observed on the other two models.

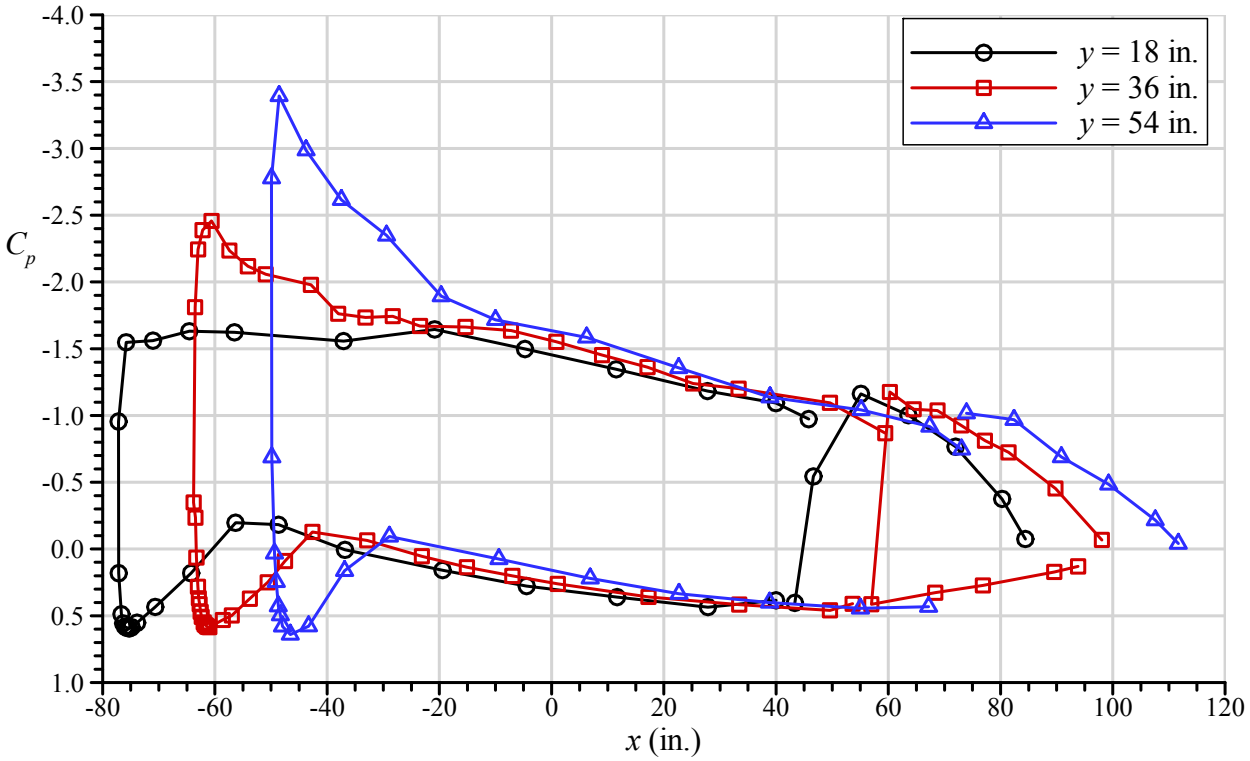

Figure 13.—Surface pressure distribution on Inboard model at, α = 3.7 deg., Flap = 13.7 deg., 140 knots and total temperature = –11.9 °C.

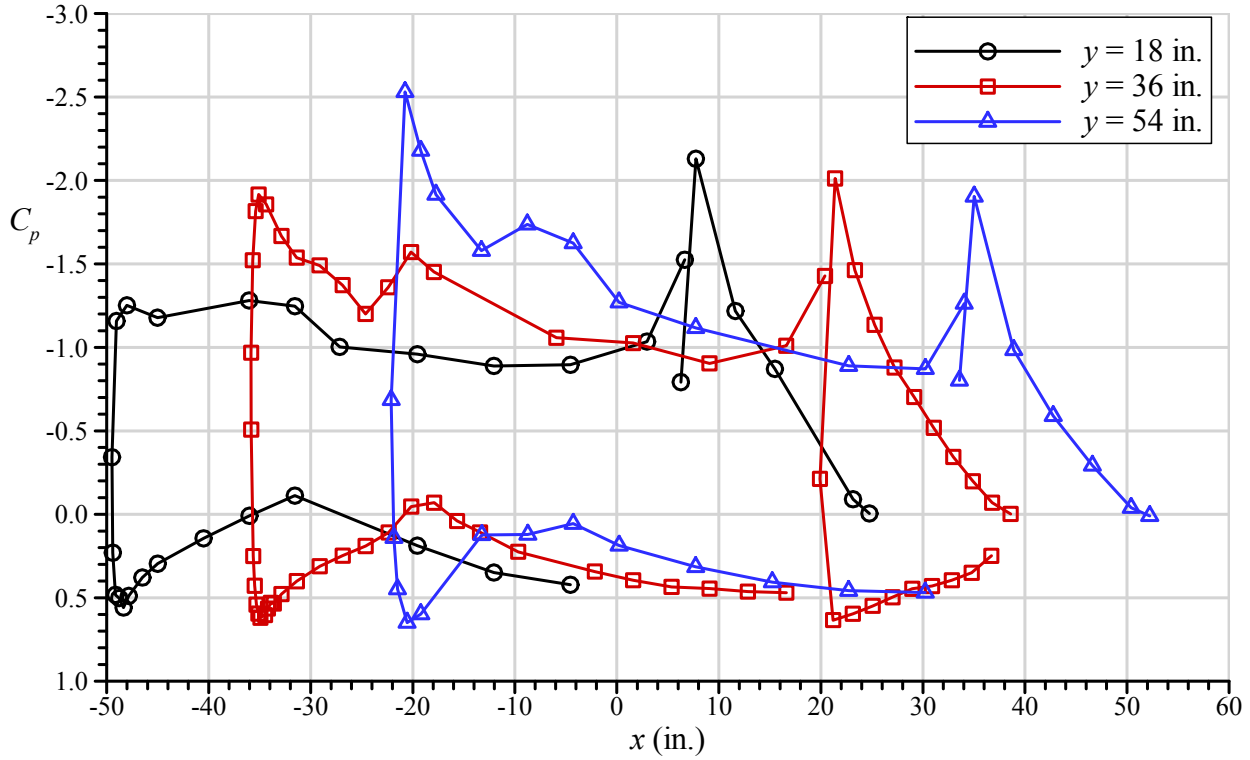

Figure 14.—Surface pressure distribution on Midspan model at, α = 3.7 deg., Flap = 25 deg., 130 knots and total temperature = –9.2 °C (from April 2015).

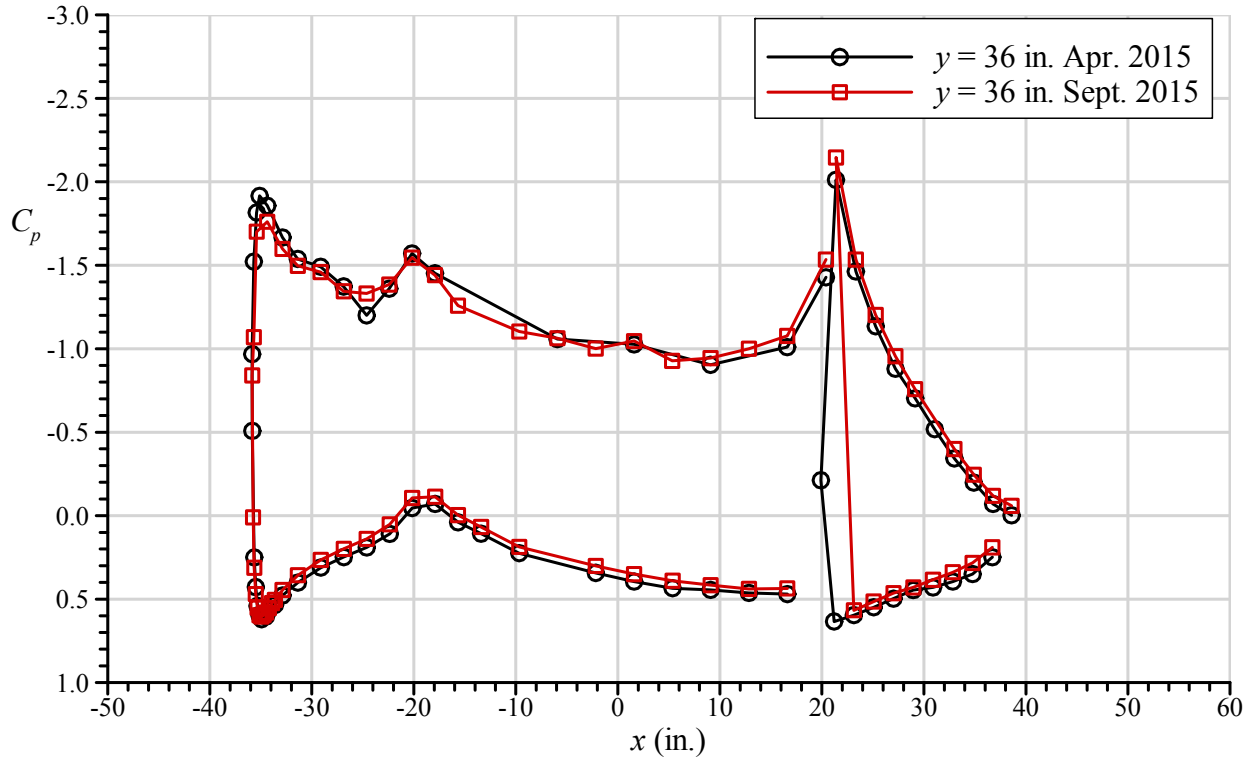

Figure 15.—Comparison of surface pressure distribution on Midspan model acquired in April 2015 and September 2015 at, α = 3.7 deg., Flap = 25 deg., 130 knots and total temperature = –9.2 °C.

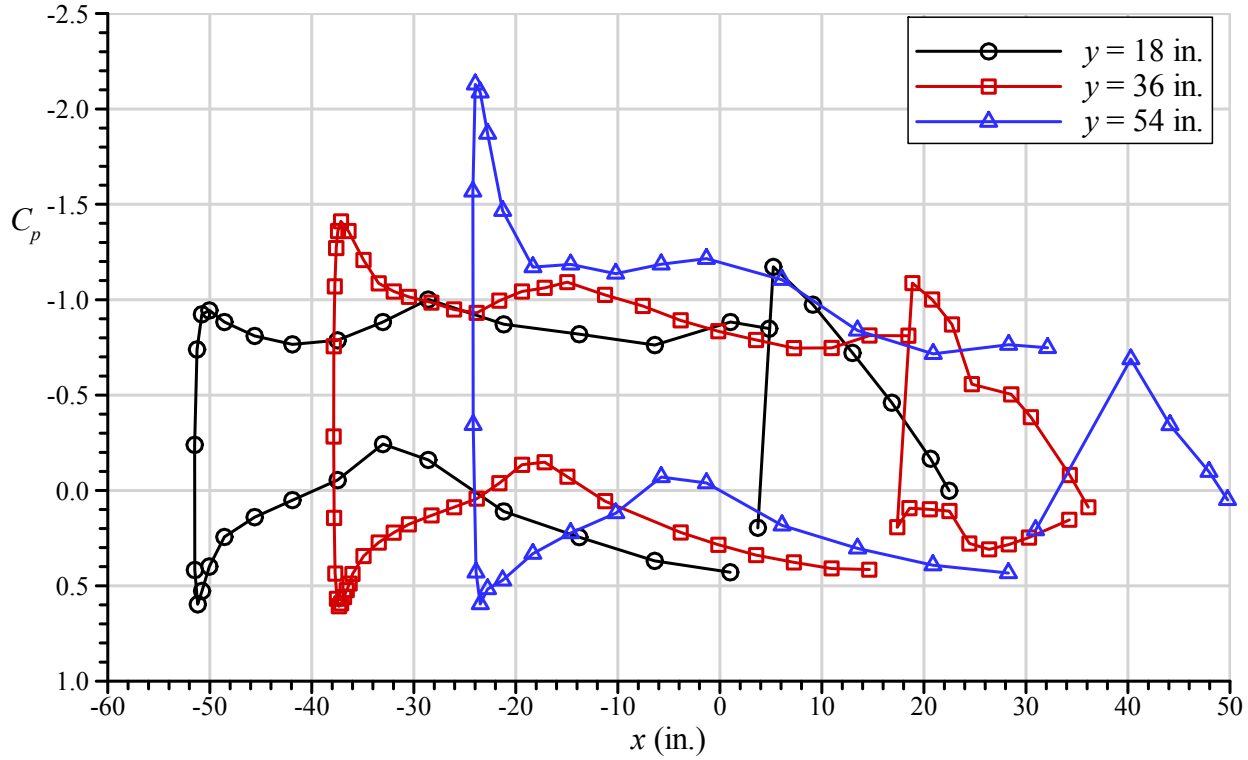

Figure 16.—Surface pressure distribution on Outboard model at, α = 3.7 deg., Flap = 14 deg., 130 knots and total temperature = 11.0 °C.

C. Flow-Visualization Results

Surface oil flow visualization was performed for the Inboard and Midspan models to determine the extent of any large-scale separated flow regions that may have adversely affected the aerodynamic performance of the hybrid models. Images are shown in Figure 17 for the Inboard model for the WB33 case at α = 3.7 deg. and flap angle = 13.7 deg. Close inspection of the oil flow lines indicated that no boundary-layer separation or reverse flow occurred over nearly all of the upper surfaces of the main element and flap. There was a region of highly 3-D flow near the leading edge at the junction of the model and test-section ceiling. As indicated in Figure 17, this area was located between the pressure tap row at y = 54 in. and the ceiling and therefore was not captured in the pressure profiles shown previously in Figure 13. The close-up image of this region appears to show movement of the surface oil away from the gap between the top of the model and ceiling in a direction toward the floor of the test section. This surface flow then merged with the downstream flow. It is likely that this flow scenario would have included some flow separation along the test-section ceiling in the same location. However, this was not investigated since the model surface flow was clearly acceptable for the objectives of this work. Fujiwara et al. (Ref. 49) provide further analysis of the flow visualization in comparison to hybrid-model CFD simulations.

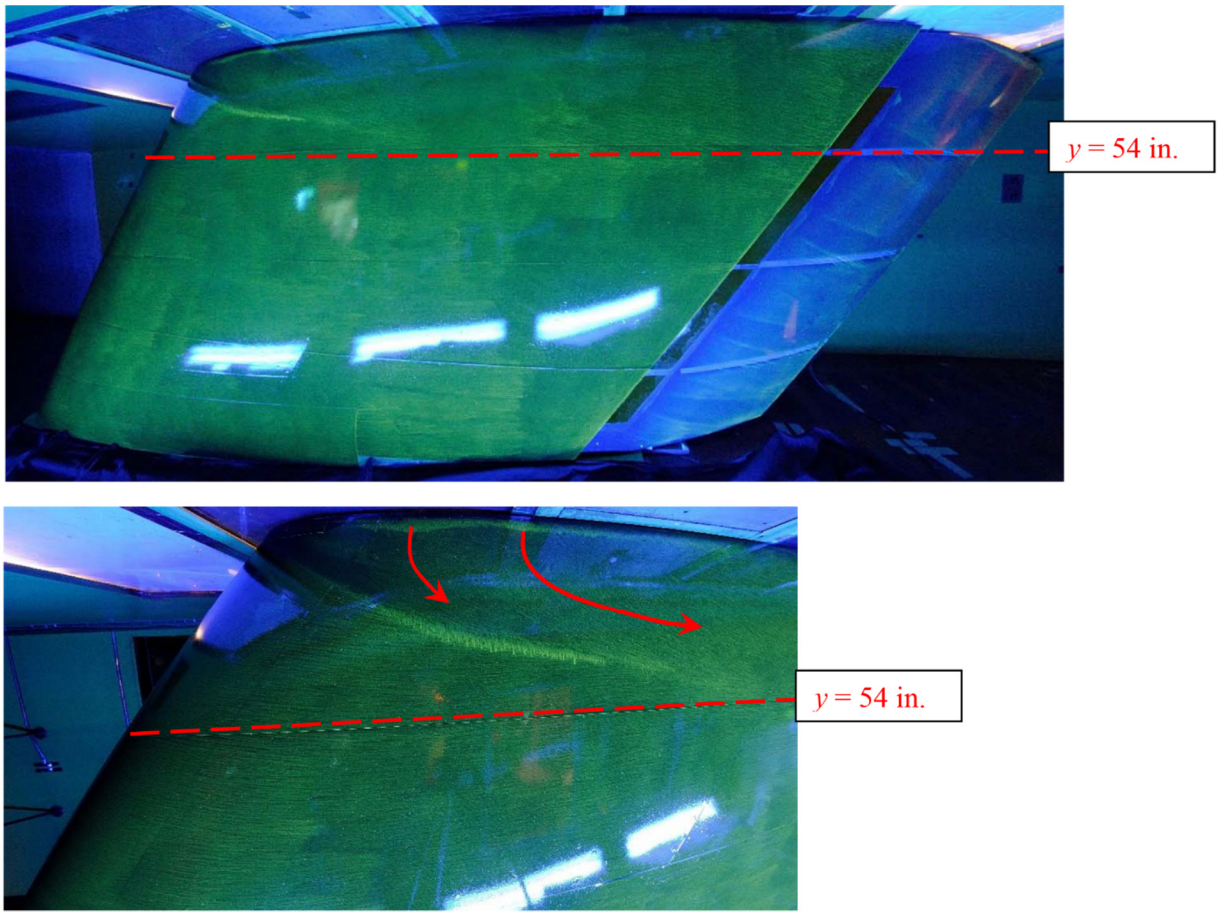

Figure 17.—Surface oil flow visualization on Inboard model, α = 3.7 deg., Flap = 13.7 deg., 130 knots and total temperature = 12.0 °C.

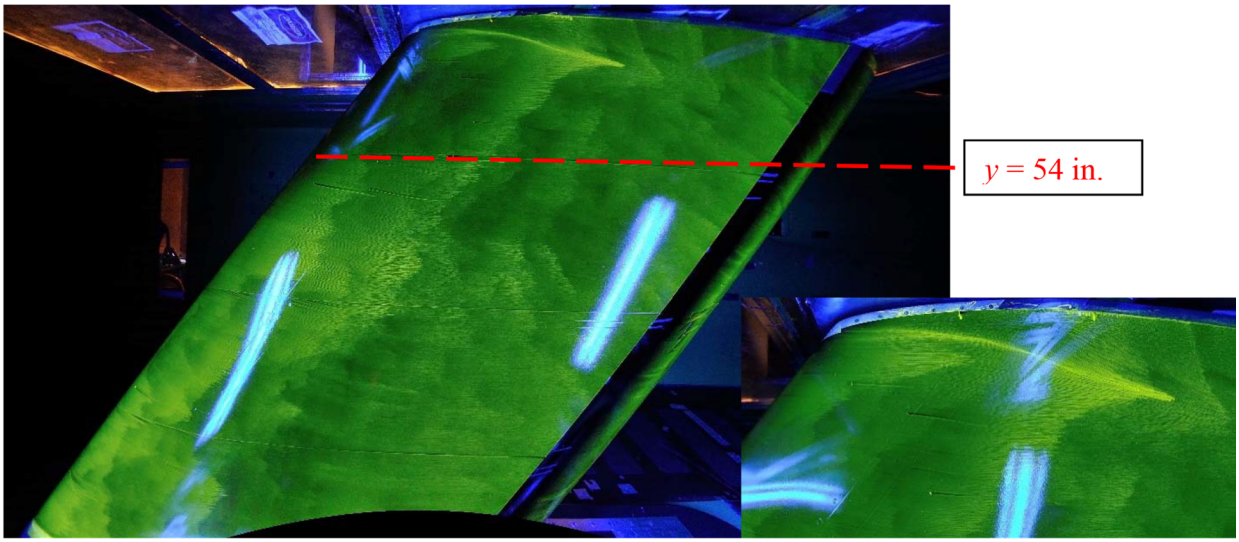

Figure 18.—Surface oil flow visualization on Midspan model, α = 3.7 deg., Flap = 25 deg., 130 knots and total temperature = 12.0 °C.

The flow visualization results for the Midspan model are shown in Figure 18 for the WB33 case at α = 3.7 deg. and flap angle = 25 deg. Close inspection of the oil flow lines indicated that no boundary-layer separation or reverse flow occurred over all of the upper surfaces of the main element and flap. The only flow feature that indicated a small degree of 3-D flow was located near the leading edge at the junction of the top of the model and the test-section ceiling. The flow through the ceiling gap appeared to generate some surface flow away from the gap in a direction toward the floor of the test section. However, this region of 3-D flow was not very large and remained close to the ceiling. This was only a minor effect as the model surface flow was clearly acceptable for the objectives of this work.

D. Ice-Accretion Results

The icing tests conducted on the three models illustrate the influence of several factors on the resulting ice accretion. For example, the results show the variation in ice accretion across the span of a large-scale swept wing from the Inboard model station at 20 percent semispan to the Outboard model station at 83 percent semispan since each model was subjected to identical icing conditions. The results show the variation in ice accretion due to a change in temperature with all other icing conditions held constant. The effects of angle of attack, drop size and liquid water content were also documented. Results obtained for the Midspan and Outboard models show the effect of the velocity-based scaling method since these models were operated near the reference speeds shown in Table 2. The presentation of the icing results is organized in this way.

1. Temperature and Drop Size Effects

The effect of temperature on the ice accretion characteristics is illustrated for each of the three models in Figures 19 to 21 for Run ID 2, 3, 4, 5, 6, 7 and 8. In each figure, the Maximum Combined Cross Section (MCCS) of the ice accretions are distributed across three plots for clarity. The MCCS for total temperatures of –6.3 and –11.2 °C are shown in two of the plots in order to compare the relative sizes of the ice shapes. Also included in each figure are photographs of the ice accretion for three selected cases. The photographs were taken looking downstream at the model leading edge, with the upper surface to the right side of each image. Beginning with the Inboard model in Figure 19, the photographs depict significant morphological changes in the ice across this range of temperature. For example, the coldest temperature (T_0 = –23.8 °C) corresponded to rime ice with the maximum thickness located near the

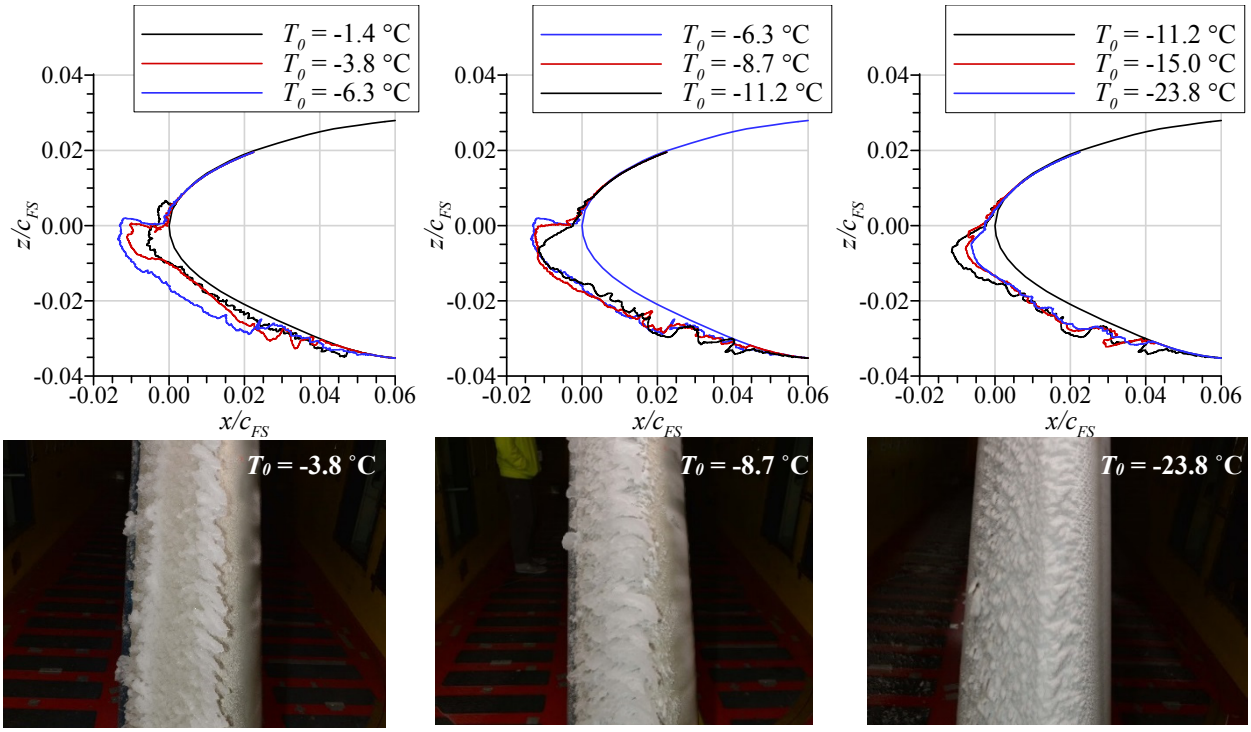

Figure 19.—MCCS and photographs of ice accretion on the Inboard model at various total temperatures with other conditions from Table 3 Run ID's 2, 3, 4, 5, 6, 7, and 8.

attachment line region. For a total temperature of –8.7 °C, the ice accretion exhibited the classic scallop or lobster tail features that are well documented in previous work on swept wings (Refs. 3 to 10). Finally, at a warmer temperature (T_0 = –3.8 °C) the maximum ice thickness was located on the upper-surface side of the attachment line which is analogous to glaze-horn type ice with a thin and smoother ice morphology in the attachment line region. This last case was referred to as the "venetian blind" condition since the spanwise-running row of ice features on the upper surface look like the slats in a venetian blind window shade. In all cases, the ice accretion was highly 3-D.

The MCCS data in Figure 19 show that the "largest" ice shape was documented at a total temperature of –6.3 °C. In this case, the "largest" ice shape was defined in terms of the maximum ice thickness measured from the clean wing surface based upon the MCCS. This condition was referred to as "maximum scallop" due to this large MCCS and high-degree of scallop or lobster tail geometry in the ice-accretion morphology. The ice accretions collected at slightly colder temperatures (e.g., T_0 = –8.7 °C and –11.2 °C) had scallop features that were smaller than those at T_0 = –6.3 °C and could be defined as "incomplete scallops" as suggested by Vargas (Ref. 9). The scallop conditions, with total temperatures in the range of –6.3 to –11.2 °C typically showed the largest cross-sections. As the temperature was decreased further, the gaps between the ice features diminished significantly, resulting in a more solid rime-type ice accretion.

Selected ice-accretion photographs and MCCS plots for the Midspan model at identical icing conditions are presented in Figure 20. The images illustrate similar variations in the ice-accretion morphology as a function of total temperature. The ice accretion for the T_0 = –3.8 °C condition did not clearly exhibit the "venetian blind" slat features that were observed for the Inboard model. The Midspan model ice accretion did not have a well-defined attachment line region for this condition, making it more difficult to define these upper-surface features. The MCCS for this condition shows that there was a significant thickness of ice in the attachment line region compared to the Inboard model. The ice accretion images at the other two temperatures (T_0 = –8.7 and –23.8 °C) were much more similar to those

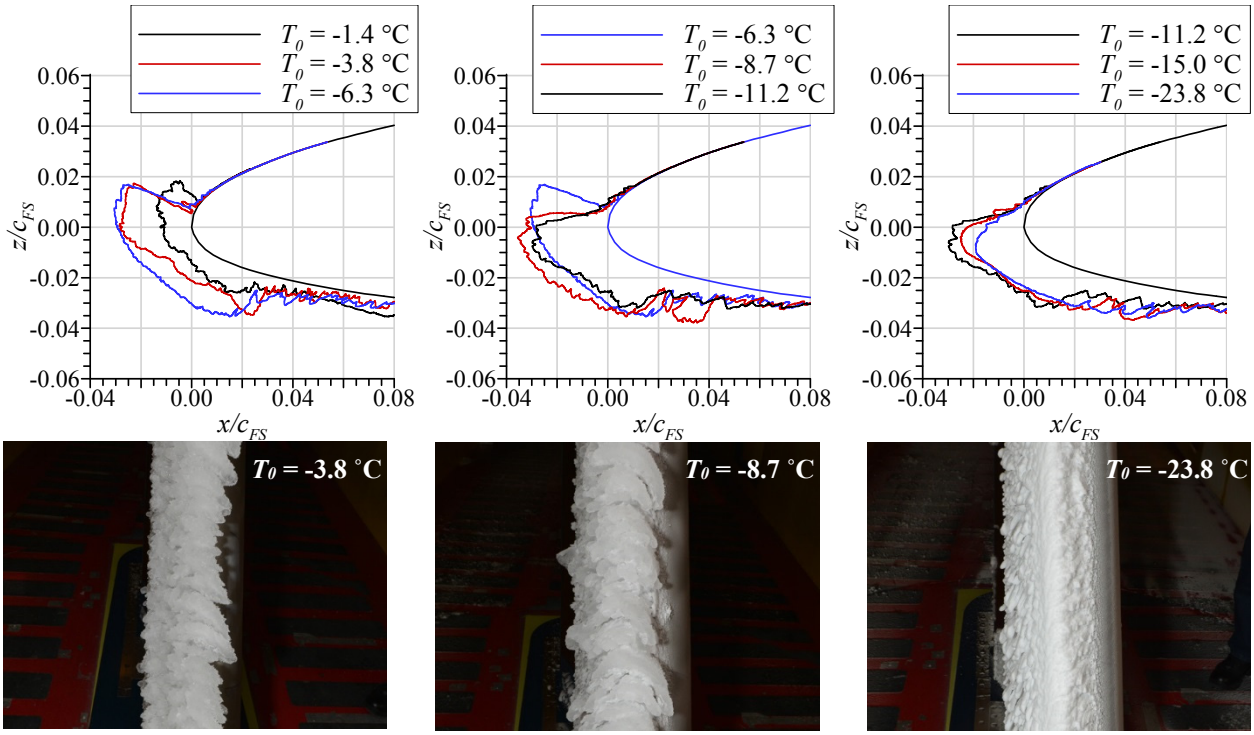

Figure 20.—MCCS and photographs of ice accretion on the Midspan model at various total temperatures with other conditions from Table 3 Run ID's 2, 3, 4, 5, 6, 7, and 8.

for the Inboard model. The plots of MCCS in Figure 20 showed that the largest ice shapes were acquired with total temperatures in the range of –3.8 to –11.2 °C. However, there were distinct changes in the ice morphology with the accretion at T_0 = –6.3 °C having the largest and most clearly defined scallop features. The gaps between the individual scallops began to close with the ice accretion becoming more solid as the total temperature was decreased from –6.3 °C.

Similar observations were made for the Outboard model data summarized in Figure 21 for the variation in total temperature. For this model, the ice-accretion morphology shown at T_0 = –3.8 °C did not contain any of the "venetian blind" type structures observed on the Inboard model in Figure 19. The MCCS plots show that the largest ice shapes were acquired with total temperatures of –6.3 and –8.7 °C.

The effect of wing spanwise location on ice accretion can be observed looking across the data in Figures 19 to 21. The photographs indicate that the general ice morphology in terms of scallop features (e.g., for T_0 = –8.7 °C) was similar for all three models. The location of the main ice shape was different for each model owing to the local aerodynamic angle of attack. Since the Inboard model had the highest local angle of attack, the main ice shape was located on the lower-surface side of the leading-edge hilite, whereas for the Midspan and Outboard models the main ice shape was located much closer to the hilite. In terms of maximum ice thickness, the normalized values for the Outboard model ($\approx 0.045c_{FS}$) were about three times larger than for the Inboard model ($\approx 0.015c_{FS}$). This is approximately the same as the ratio of the local full-scale chord lengths (297.9/91.3 = 3.3) meaning that the dimensional ice thicknesses were similar. The normalized values of maximum ice thickness for the Midspan model ($\approx 0.035c_{FS}$) were about 2.3 times larger than for the Inboard model ($\approx 0.015c_{FS}$). This too follows the ratio the local chord lengths (297.9/122.7 = 2.4) indicating similar values of dimensional ice thickness for each wing section.

The results of the total temperature variation shown in Figures 19 to 21 were used to identify the "maximum scallop" condition associated with Run ID 4 in Table 3. A number of parametric studies were conducted about this condition in order to understand the effect of such variation on the MCCS and scallop formation. For example, Run ID 14 and 15 were conducted at the same incidence and flap angles

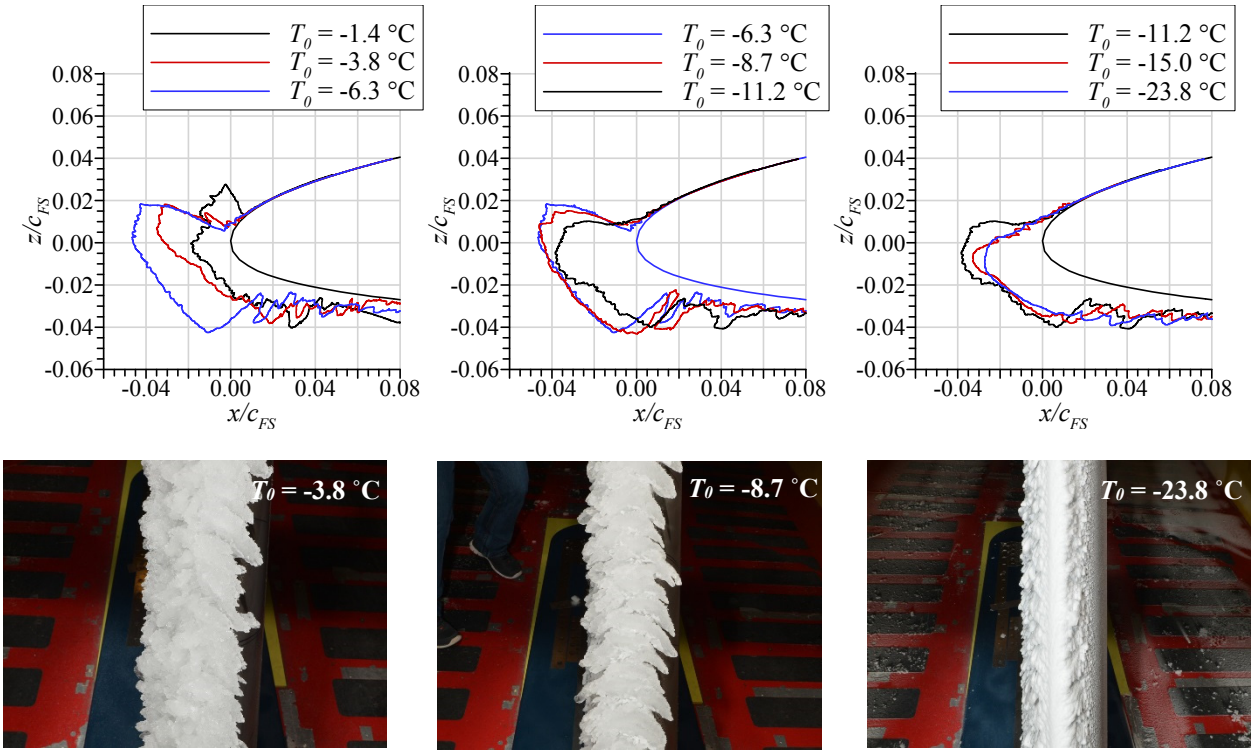

Figure 21.—MCCS and photographs of ice accretion on the Outboard model at various total temperatures with other conditions from Table 3 Run ID's 2, 3, 4, 5, 6, 7, and 8.

and airspeed as Run ID 4, but with lower MVD = 20 μm (compared to 25 μm for Run ID 4). The temperatures, LWC and exposure times were adjusted to match the freezing fraction at the attachment point and the product of the local collection efficiency at the attachment point and the accumulation parameter. The resulting MCCS are shown for each of the three models in Figure 22. The general shape of the MCCS were similar for the three run conditions with the largest variation in cross-sectional shape observed for the Midspan model. The photographs shown in Figure 22 are for the Midspan model and indicate some differences in the scallop feature formation. For Run ID 15, the scallop features were very well defined with large gaps visible on the upper-surface (right) side of the image. This is contrasted with the image for Run ID 14, where the scallop features were much smaller in scale. The image for Run ID 4 shows scallop features and gaps of a size and spatial frequency between Run ID 14 and 15. An investigation into the microphysical phenomena associated with these results was beyond the scope of these test campaigns. The data were generated for use in the development and validation of icing simulation tools consistent with the overall goals of this research effort.

2. Angle of Attack Effects

The effect of model angle of attack was investigated at the maximum scallop condition associated with Run ID 4 that was conducted at α = 3.7 deg. The resulting MCCS for each model are shown in Figure 23 also with photographs from the Midspan model. The cross-section plots confirm the expected result that the main ice shape was located closer to the leading-edge hilite for the lowest angle of attack (2.1 deg.) and that the main ice shape was located farther from the hilite for the highest angle of attack (4.4 deg.). The ice-accretion photographs on the Midspan model show a change in the scallop morphology with angle of attack. For α = 2.1 deg., the scallop features and gaps were more symmetric between the lower-surface (left) and upper-surface (right) sides of the leading edge. This is contrasted with the higher angle of attack cases at α = 3.7 and 4.4 deg. where the scallop features were angled down toward the floor on the upper-surface (right) side of the leading edge. There were also larger gaps between the scallop features observed at α = 3.7 and 4.4 deg.

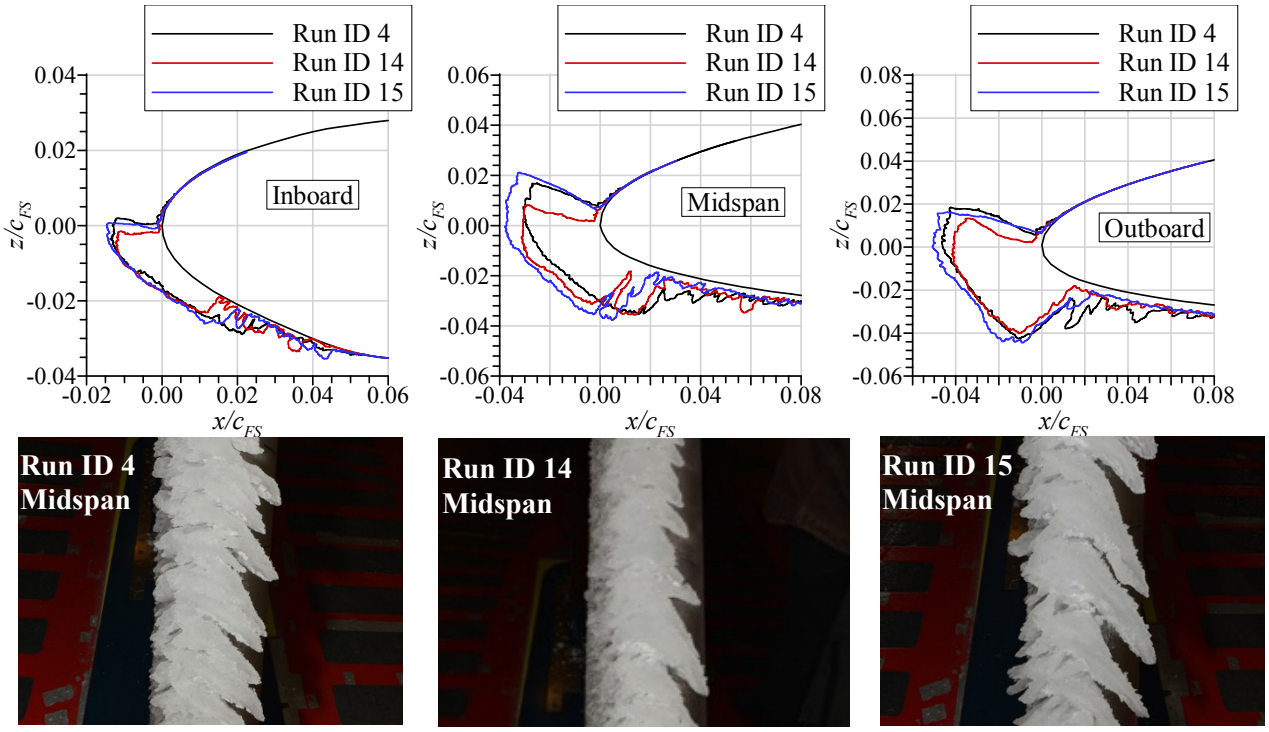

Figure 22.—MCCS and photographs of ice accretion on Midspan model showing comparison of cloud MVD and LWC effects on maximum scallop conditions (cf. Table 3).

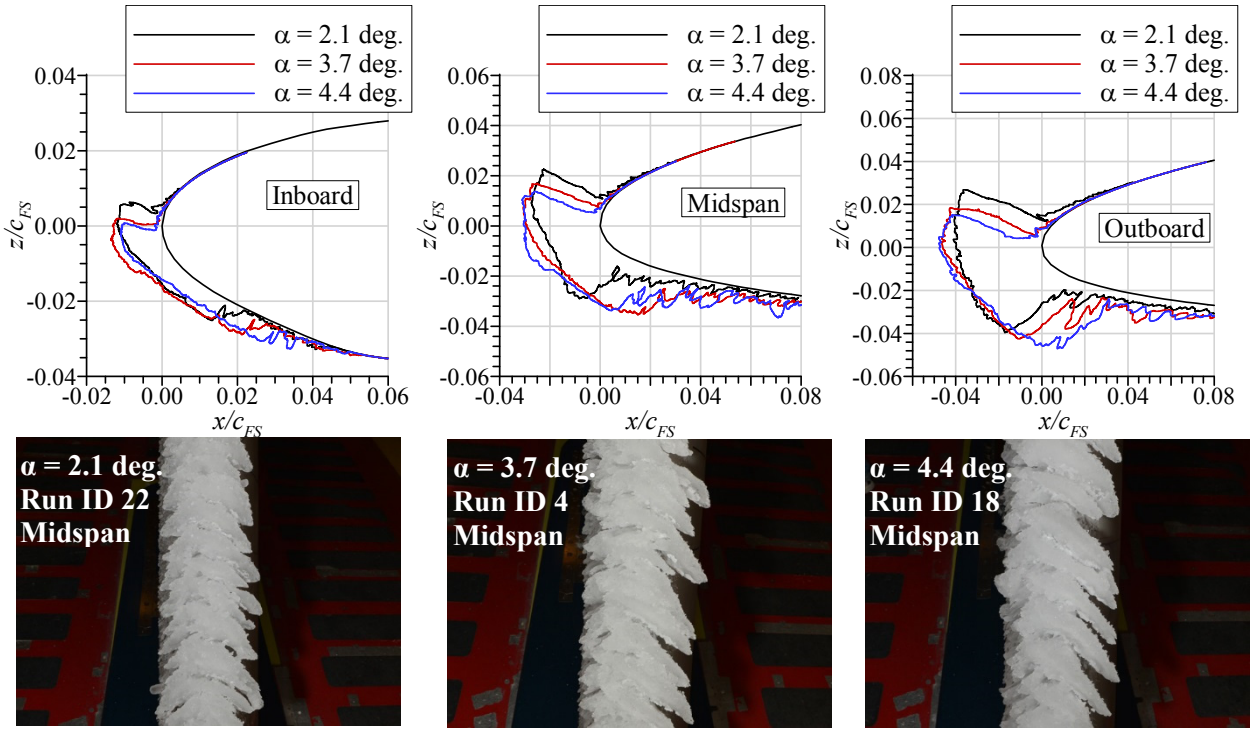

Figure 23.—MCCS and photographs of ice accretion on Midspan model showing comparison of angle of attack effects on maximum scallop condition (cf. Table 3).

In the development of the hybrid model design method discussed in Section II, Wiberg et al. (Refs. 36 and 37) suggested that matching of the attachment point location as defined by the maximum C_p, was of primary importance for ice-accretion matching between the hybrid model and full-scale wing. In fact, the authors concluded that using a higher angle of attack combined with a lower flap angle on the hybrid model was an attractive alternative approach to reduce the overall aerodynamic loads and potential for boundary-layer separation. There was an added benefit to decreasing the spanwise variation in the attachment line location. While a detailed exploration of this alternative was beyond the scope of the IRT test campaigns, one icing case at the maximum scallop condition was explored on the Midspan model. During the aerodynamic calibration, it was determined that an angle of attack of 7.5 deg. with a flap angle of 0 deg. provided for matching of the attachment point location as shown in Figure 10 for α = 3.7 deg., and flap angle = 25.0 deg. A comparison of the pressure distributions for both configurations at the 36 in. station is shown in Figure 24. The plot confirms that there was a good match of the pressures in the

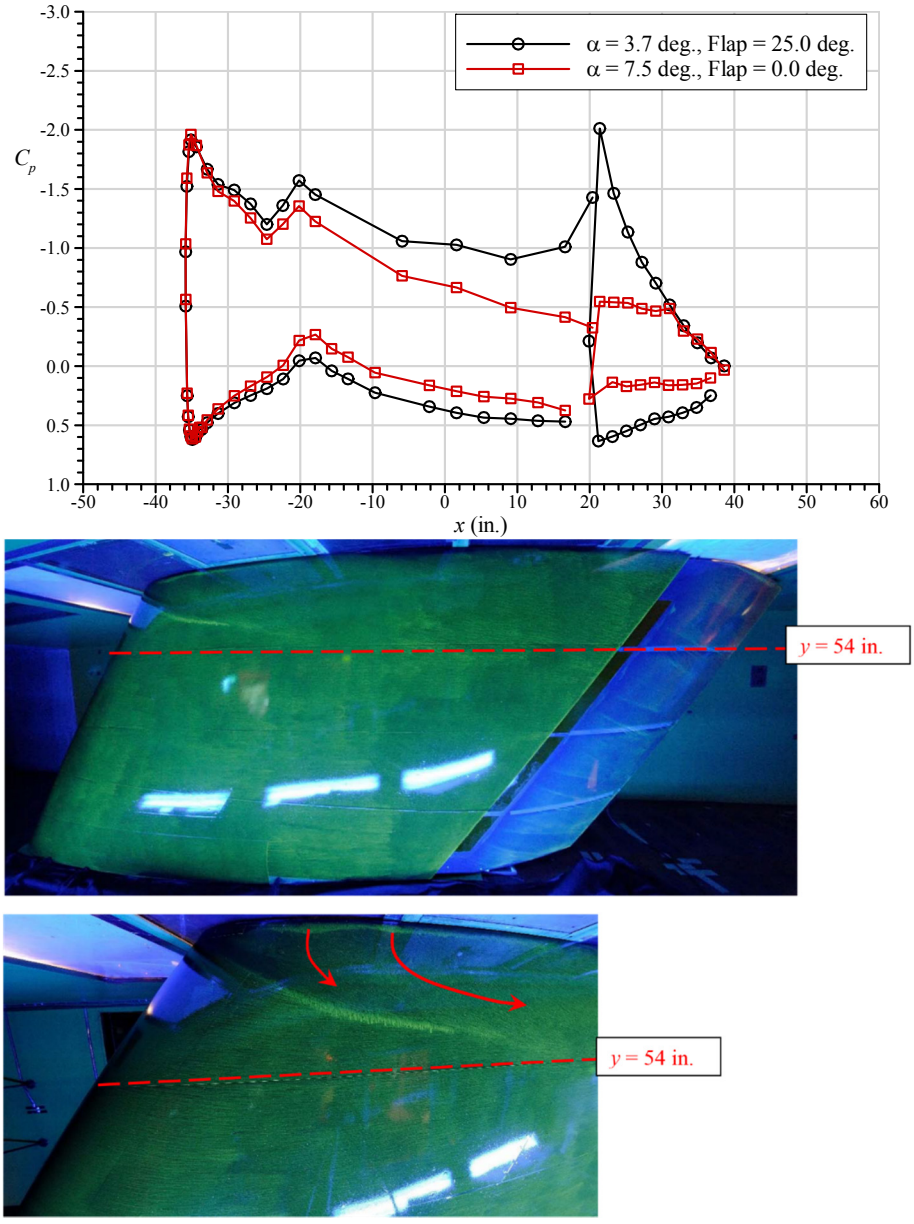

Figure 24.—Midspan model pressure distribution for alternative incidence and flap angles. Data were acquired at 130 knots and total temperature = –9.2 °C.

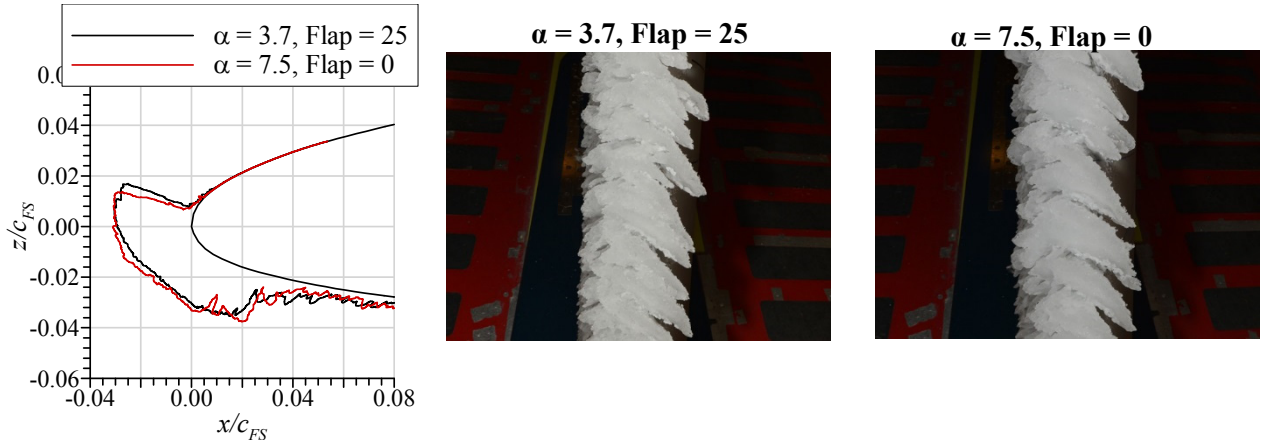

Figure 25.—Midspan model MCCS and photographs of ice accretion comparison of maximum scallop condition with attachment point matched at two different angles of attack; α = 3.7 deg., Flap = 25 Run ID 4 and α = 7.5 deg. Flap = 0 deg. Run ID 31 at identical icing conditions.

leading-edge region including the attachment point. Over the remainder of the main wing and flap, the α = 7.5 deg., flap angle = 0.0 deg. configuration had significantly reduced sectional lift as predicted by Wiberg et al. (Refs. 36 and 37). Identical icing conditions were run for each configuration and these results are shown in Figure 25. Both the MCCS shapes and photographs illustrate excellent agreement. These results support the conclusion of Wiberg et al. (Refs. 36 and 37) for the one case that was tested.

3. Flight Reference Conditions and Velocity Scaling Effects

In the description of the test matrix in Section III.C, it was noted that the IRT test conditions were simplified from the flight reference conditions in Table 2 in order to be more useful to icing-simulation code development and validation. The result was that most of the test conditions in Table 3 departed from the App. C envelope used for icing certification. The Run ID 23 case shown in Table 3 was a direct scaling of the App. C-based WB33 T-6 flight reference condition in Table 2. The MCCS results for this case are plotted against the maximum scallop condition (Run ID 4) in Figure 26 for comparison. The cross-sectional shapes were actually quite similar with the App. C-based (Run ID 23) case being slightly larger. Also shown in Figure 26 are photographs taken on the Midspan model. There was a clear difference in the morphology with the App. C-based conditions (Run ID 23) lacking the distinct scallop features. This was most likely due to the warmer total temperature = –3.1 °C for this condition that was similar to the T_0 = –3.8 °C result shown previously in Figure 20 for the Midspan model.

This condition was explored further with the Midspan model at higher speeds. The objective was to run conditions similar to the WB33 T-6 flight reference case from Table 2. While the Midspan model could be run at the reference speed of 231 knots, the air density associated with the flight-level altitude could not be matched in the ground-based IRT. The result was that the ice accretion was subjected to much higher dynamic pressure than in flight. The high dynamic pressure caused the ice accretion to shed from the model after growing to some critical thickness. The ice shedding was mitigated by reducing the airspeed from 231 to 180 knots and the exposure time from 45 to 32 min. While the airspeed of 180 was closer to the reference speed, scaling was still required for the icing conditions and these values are given as Run ID 32 in Table 3. The conditions for Run ID 23 discussed in the previous paragraph were repeated, but with the reduced exposure time of 32 min and called Run ID 23.1 in Table 3. The MCCS results are plotted in Figure 27 along with corresponding photographs of the ice accretion. The ice accretion for the higher speed condition had a larger cross section and more clearly defined scallop features thus indicating some significant differences. The differences in velocity-scaled ice-accretion results were consistent with past research reported by Anderson (Ref. 48) on a model with zero sweep. More recently, Tsao (Ref. 50) found similar difficulties in velocity scaling of ice accretion on a swept NACA 0012 wing in warmer conditions associated with glaze and scallop ice accretion.

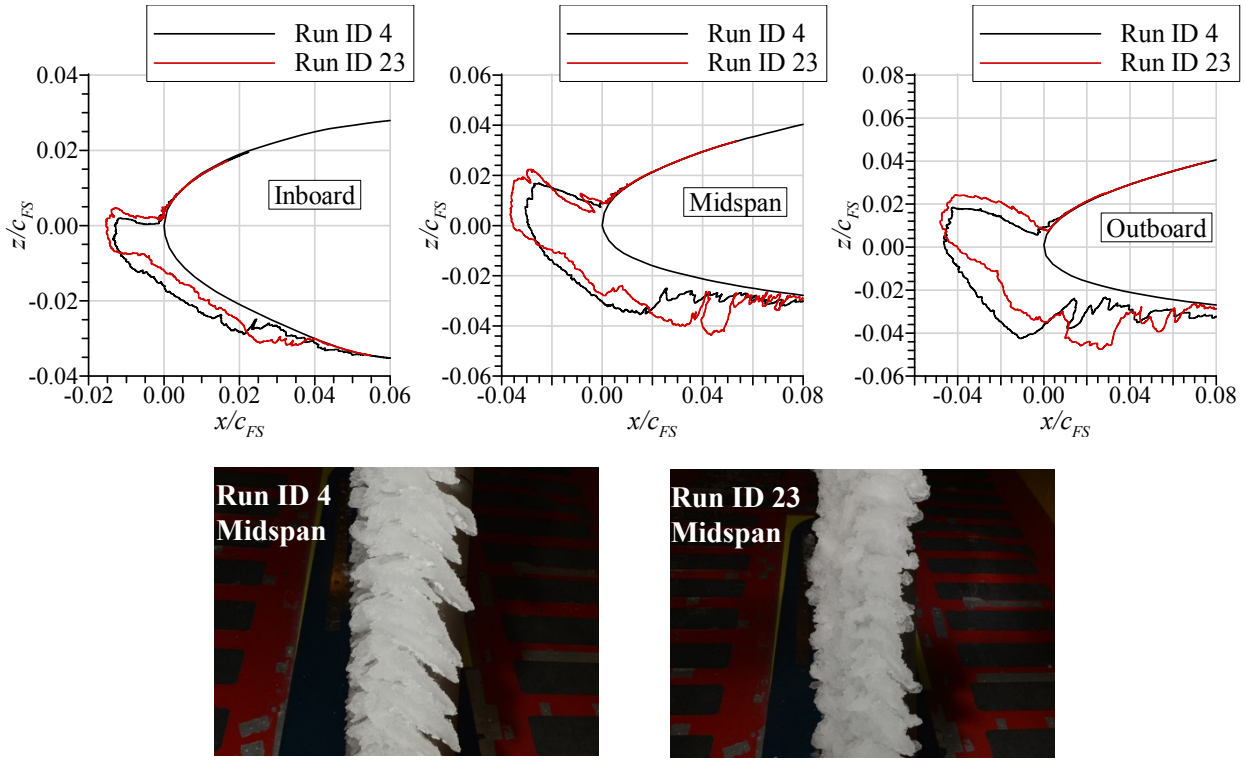

Figure 26.—MCCS and photographs of ice accretion on Midspan model showing comparison of maximum scallop condition (Run ID 4) to App. C scaled condition (Run ID 23) (cf. Table 3).

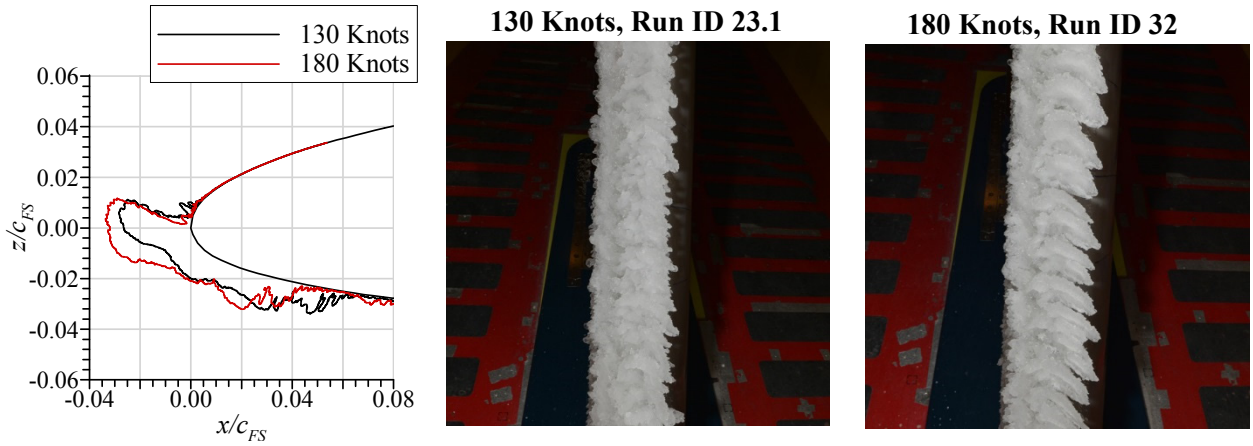

Figure 27.—Midspan model MCCS and photographs of ice accretion showing effect of airspeed on scaled ice accretion; 130 knots Run ID 23.1 and 180 knots Run ID 32.

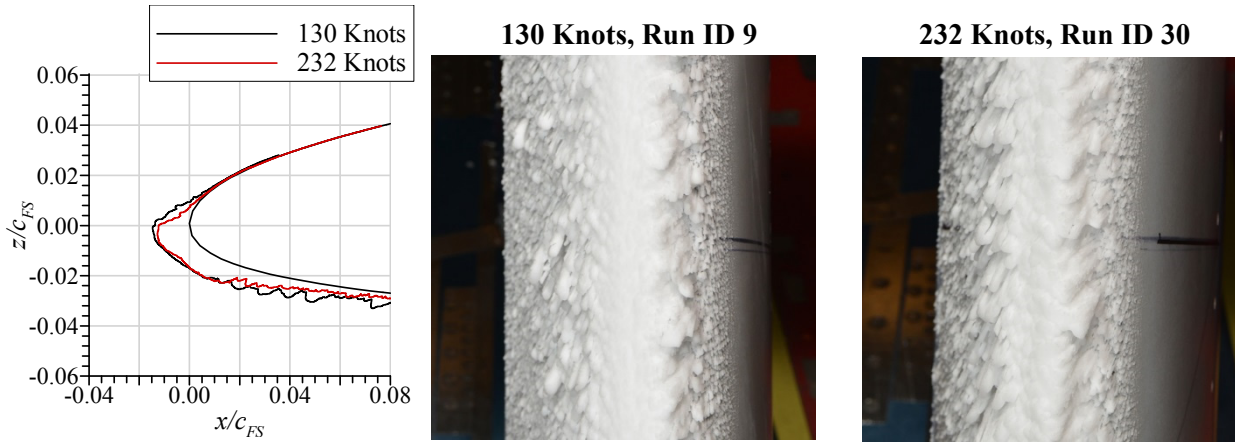

Figure 28.—Outboard model MCCS and photographs of ice accretion showing effect of airspeed on scaled ice accretion; 130 knots Run ID 9 and 232 knots Run ID 30.

The effect of velocity was also explored for rime-icing conditions to confirm that the scaling difficulties were primarily associated with glaze or scallop conditions. The results are summarized for the Outboard model in Figure 28 for the Run ID 9 conditions at 130 knots and the Run ID 30 conditions at 232 knots. In this case, the Run ID 30 conditions can be considered close to the reference conditions of WB33 T-25 in Table 2. The conditions are not identical because of limitations on the IRT ability to produce very low LWC. Also, it was not necessary to run a static temperature as low as –25 °C to generate rime ice. Aside from these adjustments, the scaled equivalent conditions are shown for 130 knots in Table 3 Run ID 9. The good comparison of the MCCS shapes and photographs in Figure 28 confirm that the velocity effects can be successfully scaled for rime ice on a swept wing.

An additional effect of velocity on ice accretion exists in some cases at temperatures near freezing. “Beak ice” (Ref. 51) has been documented to form at higher Mach numbers where there is a significant difference between the total and static temperatures. A limited number of beak ice conditions were explored to document these cases providing additional information for icing-simulation code development and validation. Example results are provided in Figure 29 for the Outboard model with Run ID 34 in Table 3. The Mach number was approximately 0.4 with a total temperature of 1.2 °C and static temperature of –6.8 °C. As shown in the photograph, there was no ice on the model in the region of the attachment line. A spanwise-running ridge of ice was observed on the upper surface corresponding to the location of minimum pressure where the local temperature was below freezing. A small amount of ice was also observed on the lower surface. The upper-surface ridge had significant variations in height above the surface along the span and was subject to shedding at the high dynamic pressures in the IRT.

The limited number of runs conducted at higher speed conditions resulted in significant findings. The results confirmed the difficulties associated with velocity-scaled conditions. The data suggest that there are morphological characteristics of glaze and scallop ice accretion on these swept-wing models that are dependent upon the velocity. However, it is often not practical to conduct the ice-accretion test at the flight reference velocity because of the high likelihood of ice shedding. It is assumed that shedding could be mitigated in an icing tunnel with altitude simulation capability due to the lower dynamic pressures, but the authors are unaware of any specific evidence to this effect. Testing near the flight reference speed is important at total temperatures near freezing in order to generate representative ice accretion dependent upon local static temperature near the leading edge. This beak ice also tends to be very susceptible to shedding that limits the testing that can be performed in ground-based facilities.

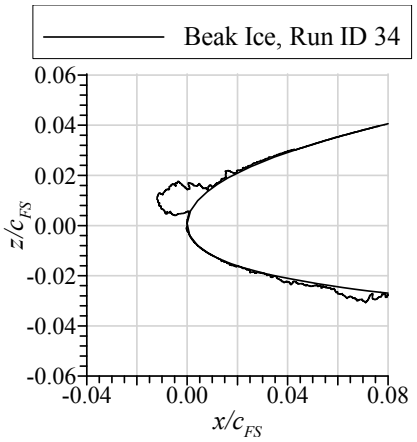

Beak Ice, Run ID 34

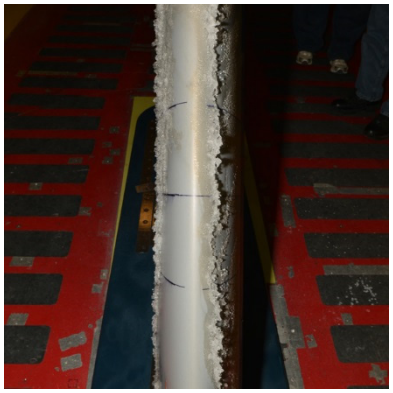

Figure 29.—Outboard model MCCS and photograph for beak ice case; Run ID 34.

V. Summary and Conclusion

Icing simulation tools and computational fluid dynamics codes are reaching levels of maturity such that they are being proposed by manufacturers for use in certification of aircraft for flight in icing conditions with increasingly less reliance on natural-icing flight testing and icing-wind-tunnel testing. Sufficient high-quality data to evaluate the performance of these tools is not currently available. This paper describes ice-accretion test results that are a part of a larger overall research effort to assess the icing and aerodynamic characteristics on large-scale, swept wings. The specific objective of this work was to generate a database of ice-accretion geometry that can be used for development and validation of icing simulation tools as well as for aerodynamic testing.

Three large-scale swept wing models were built and tested at the NASA Glenn IRT. The models represented the Inboard station (20 percent semispan), Midspan station (64 percent semispan) and Outboard station (83 percent semispan) of a wing based upon a 65 percent scale version of the Common Research Model (CRM). Owing to the large size of the reference wing, the IRT model utilized a hybrid design that maintained the full-scale leading-edge geometry with a truncated afterbody and flap. The full-scale leading-edge geometry extended downstream to 6 to 12 percent of the local chord, depending upon the wing section. The truncated afterbody and flap were designed to provide for matching the full-scale attachment point, collection efficiency and ice shape to the full-scale reference airplane.

The models were instrumented with surface pressure taps in order to acquire sufficient aerodynamic data to verify the hybrid model design capability to simulate the full-scale wing section. Pressure measurements were performed for a large range of incidence and flap angles in order to identify the attachment point location as defined by the maximum surface pressure at the model centerline. The objective of this process was to determine the appropriate flap angles that were required to match the flight reference attachment point for three flight cases. Surface pressure data were also acquired in three spanwise rows covering the main element and flap. These data indicated that the flow was well-behaved with little or no flow separation over the center section of each model. Surface oil flow visualization was also performed over the entire upper surface of the main element and flap for the Inboard and Midspan models. The flow visualization did indicate some highly 3-D flow near the model leading edge at the junction of the model and the test-section ceiling. However, this was confined to a small area and did not adversely affect the model performance for the ice-accretion tests.

The majority of each test campaign was dedicated to icing tests with a matrix of conditions that was adapted from a set of flight reference conditions. A number of simplifications were made to the icing conditions to make them more suitable for icing-simulation code development and validation. In addition, the conditions were scaled to account for a significant difference in test velocity from the flight reference velocity. The large size of the Inboard hybrid model limited the maximum velocity for icing tests to

130 knots while the flight reference velocities were in the range of 217 to 263 knots. An objective of this work was to characterize the ice accretion across the span of a full-scale swept wing. This objective required that identical icing conditions be used for all three models. However, the Midspan and Outboard model could be operated at higher speeds and were therefore used to assess the effect of the velocity scaling. For all of the ice-accretion tests, the ice geometry was measured using a 3-D scanning system in addition to photographs. In this paper, the 3-D scans were processed to extract the Maximum Combined Cross-Section (MCCS) over a 6-in. span at the model centerline that provided a 2-D description of the ice-accretion outer boundary.

A series of ice-accretion tests were conducted for each model over a range of total temperatures from –23.8 to –1.4 °C with all other conditions held constant. The results showed the changing ice-accretion morphology from rime ice at the colder temperatures to highly 3-D scallop ice in the range of –11.2 to –6.3 °C. Warmer temperatures generated highly 3-D ice accretion with glaze ice characteristics. The "maximum scallop" condition was associated with total temperature of –6.3 °C due to the large cross-section and large gaps between scallop features. The results indicated that the general ice morphology in terms of scallop features was similar for all three models. The location of the main ice shape was different for each model owing to the local aerodynamic angle of attack. Since the Inboard model had the highest local angle of attack, the main ice shape was located on the lower-surface side of the leading-edge hilite, whereas for the Midspan and Outboard models the main ice shape was located much closer to the hilite. Similar values of the dimensional maximum ice thickness were recorded for each wing section. Icing results were documented for limited parametric variations in angle of attack, drop size and cloud LWC. The effect of velocity on ice accretion was documented for the Midspan and Outboard models for a limited number of test cases. The data suggest that there are morphological characteristics of glaze and scallop ice accretion on these swept-wing models that are dependent upon the velocity. However, it is often not practical to conduct the ice-accretion test at the flight reference velocity because of the high likelihood of ice shedding. It is assumed that shedding could be mitigated in an icing tunnel with altitude simulation capability due to the lower dynamic pressures, but the authors are unaware of any specific evidence to this effect. The overall result of this work is a large database of ice-accretion geometry on large-scale, swept-wing models.

References

1. Broeren, A.P., Potapczuk, M.G., Riley, J.T., Villiedieu, P., Moens, F., Bragg, M.B., "Swept-Wing Ice Accretion Characterization and Aerodynamics," AIAA Paper 2013-2824, June 2013, also NASA TM—2013-216555, Sept. 2013.
2. Slotnick, J., Khodadoust, A., Alonso, J., Darmofal, D., Gropp, W., Lurie, E., Mavriplis, D., "CFD Vision 2030 Study: A Path to Revolutionary Computational Aerosciences," NASA/CR—2014-218178, March 2014.
3. Vargas, M., and Reshotko, E., "Physical Mechanism of Glaze Ice Scallop Formations on Swept Wings," AIAA Paper 98-0491 Jan. 1998, also NASA TM—1998-206616, Jan. 1998.
4. Vargas, M., and Reshotko, E., "Parametric Experimental Study of the Formation of Glaze Ice Shapes on Swept Wings," AIAA Paper 99-0094 Jan. 1999, also NASA TM—1999-208900, Jan. 1999.
5. Vargas, M., and Reshotko, E., "LWC and Temperature Effects on Ice Accretion Formation on Swept Wings at Glaze Ice Conditions," AIAA Paper 2000-0483 Jan. 2000, also NASA TM—2000-209777, Jan. 2000.
6. Vargas, M., Giriunas, J.A., Ratvasky, T.P., "Ice Accretion Formations on a NACA 0012 Swept Wing Tip in Natural Icing Conditions," AIAA Paper 2002-0244, Jan. 2002, also NASA TM—2002-211357, Jan. 2002.

7. Vargas, M., Papadakis, M., Potapczuk, M., Addy, H., Sheldon, D., Giriunas, J., "Ice Accretions on a Swept GLC-305 Airfoil," SAE Paper 2002-01-1519, Apr. 2002, also NASA TM—2002-211557, Apr. 2002.
8. Tsao, J.-C., "Cross Flow Effects on Glaze Ice Roughness Formation," AIAA Paper 2003-1219, Jan. 2003, also NASA/CR—2004-213086, May 2004.
9. Vargas, M., "Current Experimental Basis for Modeling Ice Accretions on Swept Wings," *Journal of Aircraft*, Vol. 44, No. 1. Jan-Feb 2007.
10. Vargas, M., "Swept Wing Icing Studies at NASA Glenn Research Center 1996-2006," SAE Paper No. 2007-01-3332, Sept. 2007.
11. Presteau, X., Montreuil, E., Leroy, A., Guffond, D., Henry, R., and Personne, P., "Experimental Study of the Scallop Formation on Swept Cylinder," SAE Paper 2007-01-3296, Sept. 2007.
12. Vargas, M., and Tsao, J.-C., "Time-Sequence Observations of the Formation of Ice Accretions on Swept Wings," AIAA Paper 2008-0470, Jan. 2008.
13. Vargas, M., and Kreeger, R.E., "Measurement of the Critical Distance Parameter Against Icing Conditions on a NACA 0012 Swept Wing Tip," AIAA Paper 2009-4123, June 2009, also NASA TM—2011-216966, Feb. 2011.
14. Tsao, J.-C., and Lee, S., "Evaluation of Icing Scaling on Swept NACA 0012 Airfoil Models," SAE Paper 2011-38-0081, June 2011, also NASA CR—2011-217419, June 2012.
15. Bidwell, C.S. and Mohler Jr., S.R., "Collection Efficiency and Ice Accretion Calculations for a Sphere, a Swept MS(1)-317 Wing, a Swept NACA-0012 Wing Tip, an Axisymmetric Inlet, and a Boeing 737-300 Inlet," AIAA Paper 95-0755, Jan. 1995.
16. Bidwell, C.S. and Potapczuk, M.G., "User's Manual for the NASA Lewis Three-Dimensional Ice Accretion Code (LEWICE3D)," NASA TM 105974, Dec. 1993.
17. Potapczuk, M.G. and Bidwell, C.S., "Swept Wing Ice Accretion Modeling," NASA TM 103114, Jan. 1990.
18. Potapczuk, M.G. and Bidwell, C.S., "Numerical Simulation of Ice Growth on a MS-317 Swept Wing Geometry," NASA TM 103705, Jan. 1991.
19. Potapczuk, M., Papadakis, M. and Vargas, M., "LEWICE Modeling of Swept Wing Ice Accretions," AIAA Paper 2003-6565, Jan. 2003.
20. Bidwell, C.S., "Icing Analysis of a Swept NACA 0012 Wing Using LEWICE3D Version 3.48," AIAA Paper 2014-2200, June 2014.
21. Beaugendre, H., Morency, F., Habashi, W.G., "FENSAP-ICE's Three-Dimensional In-Flight Ice Accretion Module: ICE3D," *Journal of Aircraft*, Vol. 40, No. 2, Mar.-Apr. 2003, pp. 239–247.
22. Nakakita, K., Nadarajah, S., Habashi, W., "Toward Real-Time Aero-Icing Simulation of Complete Aircraft via FENSAP-ICE," *Journal of Aircraft*, No. 1, Jan.-Feb., 2010, pp. 96–109.
23. Hedde, T., and Guffond, D., "Development of a Three-Dimensional Icing Code, Comparison with Experimental Shapes," AIAA Paper 92-0041, Jan. 1992.
24. Hedde, T., and Guffond, D., "Improvement of the ONERA 3D Icing Code Comparison with 3D Experimental Shapes," AIAA Paper 93-0169, Jan. 1993.
25. Presteau, X., Montreuil, E., Chazottes, A., Vancassel, X., and Personne, P, "Experimental and Numerical Study of Scallop Ice on Swept Cylinder," AIAA Paper 2009-4124, June 2009.
26. Villedieu, P., Trontin, P., Guffond, D., Bobo, D., "SLD Lagrangian Modeling and Capability Assessment in the Frame of ONERA 3D Icing Suite," AIAA Paper 2012-3132, June 2012.
27. Szilder, K., McIlwain, S., and Lozowski, E.P., "Numerical Simulation of Complex Ice Shapes on Swept Wings," ICAS Paper 2006-2.5.1, Sept. 2006.
28. Szilder, K., and Lozowski, L., "Progress Towards a 3D Numerical Simulation of Ice Accretion on a Swept Wing Using the Morphogenetic Approach," SAE Paper 2015-01-2162, June 2015.
29. Vassberg, J.C., DeHann, M.A., Rivers, S.M., and Wahls, R.A., "Development of a Common Research Model for Applied CFD Validation Studies," AIAA Paper 2008-6919, Aug. 2008.
30. Rivers, M.B., and Dittberner, A., "Experimental Investigation of the NASA Common Research Model," AIAA Paper 2010-4218, June 2010.

31. Rivers, M.B., and Dittberner, A., "Experimental Investigations of the NASA Common Research Model in the NASA Langley National Transonic Facility and the NASA Ames 11-Ft Transonic Wind Tunnel," AIAA Paper 2011-1126, Jan. 2011.
32. Vassberg, J.C., Tinoco, E.N., Mani, M., Rider, B., Zickuhr, T., Levy, D.W., Brodersen, O., Eisfeld, B., Crippa, S., Wahls, R.A., Morrison, J.H., Mavriplis, D.J., and Murayama, M., "Summary of the Fourth AIAA CFD Drag Prediction Workshop," AIAA Paper 2010-4547, June 2010.
33. Fujiwara, G.E.C., Woodard, B.S., Wiberg, B.D., Mortonson, A.J., Bragg, M.B., "A Hybrid Airfoil Design Method for Icing Wind Tunnel Tests," AIAA Paper 2013-2826.
34. Mortonson, A.J., "Use of Hybrid Airfoil Design in Icing Wind Tunnel Tests of Large Scale Swept Wings," M.S. Thesis, Dept. of Aerospace Eng., Univ. of Illinois, Urbana, IL, 2011.
35. Fujiwara, G.E.C., Wiberg, B.D., Woodard, B.S., and Bragg, M.B., "3D Swept Hybrid Wing Design Method for Icing Wind Tunnel Tests," AIAA Paper 2014-2616, June 2014.
36. Wiberg, B.D., Fujiwara, G.E.C., Woodard, B.S., and Bragg, M.B., "Large-Scale, Swept-Wing Icing Simulations in the NASA Glenn Icing Research Tunnel Using LEWICE3D," AIAA Paper 2014-2617, June 2014.
37. Wiberg, B.D., "Large-Scale, Swept-Wing Ice Accretion Modeling in the NASA Glenn Icing Research Tunnel Using LEWICE3D," M.S. Thesis, Dept. of Aerospace Eng., Univ. of Illinois, Urbana, IL, 2013.
38. Fujiwara, G.E.C., "Design of 3D Swept Wing Hybrid Models for Icing Wind Tunnel Tests," M.S. Thesis, Dept. of Aerospace Eng., Univ. of Illinois, Urbana, IL, 2014.
39. Sclafani, A.J., Slotnick, J.P., Vassberg, J.C., and Pulliam, T.H., "Extended OVERFLOW Analysis of the NASA Trap Wing Wind Tunnel Model," AIAA Paper 2012-2919, June 2012.
40. Saeed, F., Selig, M.S., and Bragg, M.B., "Hybrid Airfoil Design Procedure Validation for Full-Scale Ice Accretion Simulation," *Journal of Aircraft*, Vol. 36, No. 5, Sept.-Oct., 1999, pp. 769–776.
41. Saeed, F., Selig, M.S., and Bragg, M.B., "Hybrid Airfoil Design to Simulate Full-Scale Ice Accretion Throughout a Given α Range," *Journal of Aircraft*, Vol. 35, No. 2, Mar.-Apr., 1998, pp. 233–239.
42. Saeed, F., Selig, M.S., and Bragg, M.B., "Design of Subscale Airfoils with Full-Scale Leading Edges for Ice Accretion Testing," *Journal of Aircraft*, Vol. 34, No. 1, Jan.-Feb., 1997, pp. 94–100.
43. Steen, L.E., Ide, R.F., Van Zante, J.F, and Acosta, W.J., "NASA Glenn Icing Research Tunnel: 2014 and 2015 Cloud Calibration Procedures and Results," NASA TM—2015-218758, May 2015.
44. Soeder, R.H., Sheldon, D.W., Ide, R.F., Spera, D.A., and Andracchio, C.R., "NASA Glenn Icing Research Tunnel User Manual," NASA TM—2003-212004, Sept. 2003.
45. Lee, S., Broeren, A.P., Addy, H.E., Jr., Sills, R., and Pifer, E.M., "Development of 3-D Ice Accretion Measurement Method," AIAA Paper 2012-2938, June 2012; also NASA/TM—2012-217702, Sept. 2012.
46. Lee, S., Broeren, A.P., Kreeger, R.E., Potapczuk, M.G., and Utt, L., "Implementation and Validation of 3-D Ice Accretion Measurement Methodology," AIAA Paper 2014-2613, June 2014.
47. Broeren, A.P., Addy, H.E., Jr., Lee, S., and Monastero, M.C., "Validation of 3-D Ice Accretion Measurement Methodology for Experimental Aerodynamic Simulation," NASA/TM—2015-218724, July 2015.
48. Anderson, D.N., "Manual of Scaling Methods," NASA CR—2004-212875, Mar. 2004.
49. Fujiwara, G.E.C., Bragg, M.B., Camello, S.C., and Lum, C., "Computational and Experimental Ice Accretions of Large Scale Swept Wings in the Icing Research Tunnel," AIAA 8th Atmospheric and Space Environments Conference, Washington D.C., June 13–17, 2016 (submitted for publication), 2016.
50. Tsao, J.-C., "Velocity Effect on Swept-Wing Ice Accretion for Scaling Consideration," Oral Presentation, SAE 2015 International Icing Conference, Prague, Czech Republic, June 22–25, 2015.
51. SAE Aerospace, "Aircraft Inflight Icing Terminology," Aerospace Recommended Practice, ARP5624, April 2013.